Kinetic Modeling of the Reversible or Irreversible Electrochemical Responses of FeFe-Hydrogenases

Andrea Fasano, Carole Baffert, Conrad Schumann, Gustav Berggren, James A Birrell, Vincent Fourmond, Christophe Léger

Kinetic modeling of the reversible or irreversible electrochemical responses of FeFe-hydrogenases

Andrea Fasano[a], Carole Baffert[a], Conrad Schumann[b], Gustav Berggren[b], James A. Birrell[c], Vincent Fourmond[a], Christophe Léger[a*]

a. Laboratoire de Bioénergétique et Ingénierie des Protéines. CNRS, Aix Marseille Université, UMR 7281. Marseille. France.

b. Molecular Biomimetics, Department of Chemistry, Ångström Laboratory, Uppsala University, 75120 Uppsala, Sweden

c. School of Life Sciences, University of Essex, Wivenhoe Park, Colchester, CO4 3SQ, UK

* chistophe.leger@imm.cnrs.fr

Abstract

The enzymes FeFe-hydrogenase catalyse H_2 evolution and oxidation at an active site that consists of a [4Fe-4S] cluster bridged to a [Fe$_2$(CO)$_3$(CN)$_2$(azadithiolate)] subsite. Previous investigations of their mechanism were mostly conducted on a few "prototypical" FeFe-hydrogenases, such as that from *Chlamydomonas reinhardtii* (Cr HydA1), but atypical hydrogenases have recently been characterized in an effort to explore the diversity of this class of enzyme. We aim at understanding why prototypical hydrogenases are active in either direction of the reaction in response to a small deviation from equilibrium, whereas the homologous enzyme from *Thermoanaerobacter mathranii* (Tam HydS) shows activity only under conditions of very high driving force, a behavior which was referred to as "irreversible catalysis". We follow up on previous spectroscopic studies and recent developments in the kinetic modeling of bidirectional reactions to investigate and compare the catalytic cycles of Cr HydA1 and Tam HydS under conditions of direct electron transfer with an electrode. We compare the hypothetical catalytic cycles described in the literature, and we show that the observed changes in catalytic activity as a function of potential, pH and H_2 concentration can be explained with the assumption that the same catalytic mechanism applies. This helps us identify which variations in properties of the catalytic intermediates give rise to the distinct "reversible" or "irreversible" catalytic behaviors.

Introduction

The redox reactions of H_2 oxidation and production are catalyzed in Nature by metalloenzymes whose active sites are composed of abundant metals, Ni and Fe, and are called hydrogenases. Here we focus on FeFe-hydrogenases, whose active site, called the "H-cluster", is composed of a [4Fe-4S]$_H$ cluster, linked by a cysteine to a dinuclear Fe center ([2Fe]$_H$). The two Fe ions of [2Fe]$_H$ are coordinated by three carbonyl ligands (one of which is bridging) and two cyanides, and bridged by an amine-dithiolate (ADT) ligand. The Fe ion that is remote from the cubane is referred to as the "distal" Fe, or Fe$_d$. In the catalytic cycle, H_2 binds to the open coordination site on Fe$_d$, and it is split heterolytically into a terminal hydride and a proton. The latter binds to the nitrogen of the ADT ligand,[1,2] from where it is transferred to a nearby cysteine, and then further along a chain of acidic residues.[3,4] This proton transfer pathway is very conserved in the phylogenetic group of FeFe-hydrogenases that includes

the most studied enzymes (called group "A", or "prototypical" in ref [5]). In these enzymes, long range electron transfer may involve accessory FeS clusters.

Detailed information about the catalytic cycle has been obtained over decades of spectroscopic investigations. Some of the proposed catalytic intermediates are paramagnetic and hence detectable by electron paramagnetic resonance spectroscopy, but the spectroscopic technique that has become most popular in hydrogenase research is Fourier-transform infrared spectroscopy (FTIR), which can detect the vibrations of the CO and CN diatomic ligands to identify various states of the H-cluster. Regarding prototypical hydrogenases, two distinct mechanistic hypotheses have emerged.[6]
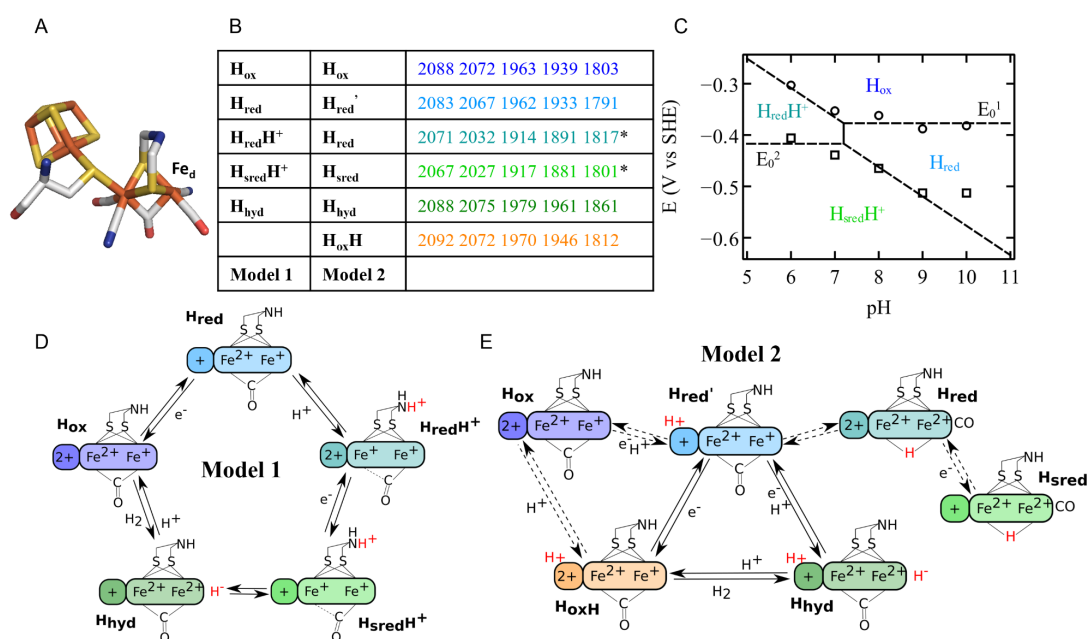

Figure 1: (A) The active site "H-cluster" of [FeFe]-hydrogenases (color code: Fe (orange), S (yellow), C (white), N (blue) and O (red)). (B) FTIR frequencies of the Cr HydA1 states in panels D and E; the states of model 1 and model 2 that share the same FTIR signature are shown with the same color. Asterisks on the vibration frequencies of $H_{red}H^+$ and $H_{sred}H^+$ mark the bridging CO frequencies detected at low temperature in ref [7] (C) Pourbaix diagram of H_{ox}, H_{red}, $H_{red}H^+$ and $H_{sred}H^+$ transitions adapted from ref [8]; (D) Model 1 of the catalytic cycle of [FeFe]-hydrogenases, proposed in ref [8]; (E) Model 2 of the catalytic cycle of [FeFe]-hydrogenases, proposed in ref [9];

The most oxidized catalytic intermediate is H_{ox}, where the electronic configuration of the dinuclear cluster is Fe(II)/Fe(I) and the cubane is oxidized (2+). In model 1 (fig. 1D), the reduction of H_{ox} at high pH produces the H_{red} state, where the cubane is reduced. H_{red} has a pK_a around 7, and at pH < pK_a, the reduction of H_{ox} is coupled to a protonation, to give the $H_{red}H^+$ state. This protonation was evidenced by the pH dependence of the reduction potential of the H_{ox} state observed in spectroelectrochemical titrations of the active site at different pH values (the corresponding Pourbaix diagram is reproduced from ref [8] in fig. 1C). The vibrational band of the bridging CO ligand is apparently lost upon protonation, suggesting that the ligand shifts to a terminal position.[10,11] However, recent data suggests

that the band is only weak and highly broadened, as low temperature measurements produce a more intense sharp band.[7,12,13] It is hypothesized that proton binding to the nitrogen of the amine in the azadithiolate ligand induces an intramolecular electron transfer from the cubane to the dinuclear cluster, which becomes Fe(I)/Fe(I). An increased electron density at $[2Fe]_H$ explains the larger red shift of the vibration bands in the H_{ox} to $H_{red}H^+$ transition than in H_{ox} to H_{red}.[8] Reduction of $H_{red}H^+$ gives the super-reduced state $H_{sred}H^+$,[14] with a protonated amine and a reduced cubane, which is a tautomer of H_{hyd}, with a hydride on Fe_d.[15–18] The second protonation of the doubly reduced state gives a series of elusive species, called $H_{hyd}H^+$ and $H_{ox}H_2$, from which the release of H_2 completes the catalytic cycle by giving back H_{ox}. Some spectroscopic signatures have been attributed to $H_{hyd}H^+$.[16,19]

In model 2 (fig. 1E), the FTIR signature assigned to the H_{red} state is instead attributed to a state called H_{red}' (panel E), and the H_{ox} to H_{red}' reaction supposedly involves the reduction and coupled protonation of the cubane. This was concluded from the pH-dependence of the potential of the cubane, measured in enzyme variants where the nitrogen atom of the amine dithiolate bridge is replaced with a carbon atom.[20] (However, this observation was recently challenged.[21]) Consistent with the above described transformation between H_{red} and $H_{red}H^+$, H_{red}' is replaced at pH below 7 with the $H_{red}H^+$ state, which is called H_{red} in model 2 (fig. 5C in ref [9]). However, at variance with model 1, it is assumed that the transition from H_{red}' to H_{red} at low pH is the result of a proton rearrangement, with a deprotonation of the cubane and the formation of a bridging hydride, and the bridging CO shifts to an apical position (something that is not supported by the spectroscopic investigations of Cr in ref [13], and not observed in any of the states of the H-cluster of *C. acetobutylicum* hydrogenase I [12]). Considering the expected stability of this bridging hydride, the H_{red} species and the corresponding H_{sred} state obtained by further reduction (which has the same spectroscopic signature as the species denoted $H_{sred}H^+$ in model 1) are considered to be off-pathway. Instead, reductive catalysis proceeds from H_{red}', whose one-electron one-proton reduction gives a hydride species also denoted H_{hyd}, but now considered protonated on the cubane in addition to Fe_d. The so-called "regulatory" proton on the cubane is retained throughout the catalytic cycle. Further steps of reduction, protonation and H_2 release give back H_{red}' bypassing the H_{ox} state, which is also considered off-pathway (see fig. 2 of ref [9]). Whether or not the spectroscopic signal assigned to $H_{ox}H$ reflects a true catalytic intermediate or an artifact is currently debated.[22,23]

Recently, two FeFe-hydrogenases whose active site environment differs significantly from that in group A have been characterized, although to a much lesser extent than group A hydrogenases. These enzymes are *Thermotoga maritima* (Tm) HydS[24] and *Thermoanaerobacter mathranii* HydS (Tam),[25] from groups C and D respectively.[26] Albeit from two distinct phylogenetic groups, the latter enzymes feature an identical set of electron relay FeS clusters and are structurally very similar. Indeed, as compared to group A enzymes, most of the altered amino acids in the direct vicinity of the H-cluster are identical in *Tam* HydS and *Tm* HydS. In the sequences of both enzymes, the cysteine residue that accepts protons from the amine dithiolate ligand in group A hydrogenases is replaced with an alanine, and none of the residues that form the proton transfer pathway in group A hydrogenases are present; a possible alternative pathway was recently identified in group D.[27] The strong similarities between Tam HydS and TmHydS suggest similar active site properties and function.

In Tm HydS, the H_{ox} FTIR signature is very similar to that of group A hydrogenases (compare fig. 1B and fig. 5A in ref [24]), but the midpoint potentials of the two one-electron redox transitions are more separated than those of Cr HydA1 (-300 and -570 mV in Tm HydS[24] versus -362 and -465 mV in Cr HydA1,[8] both at pH 8), suggesting that the half-reduced state of the H-cluster is stable over a larger potential range in Tm HydS than in Cr HydA1. How this is determined by the environment of the H-cluster is unclear.[28] Regarding Tam HydS, the H_{ox} state signature is again unremarkable, and, as is the case with Tm, the one-electron reduced state is very stable.[25]

In terms of functional properties, both Tam and Tm HydS have low activity (consistent with their putative role as H_2 sensors), but Tam HydS is also remarkable in that catalysis is only observed upon application of a large driving force for H_2 oxidation or evolution, and we assume that this is also the case of Tm HydS. This behavior, termed "irreversible catalysis",[29–32] is observed in voltammetric experiments where the enzyme undergoes direct electron transfer with an electrode and catalysis is detected as a positive or negative current (for H_2 oxidation and evolution, respectively), as the electrode potential is shifted from the Nernst potential of the H^+/H_2 couple.[33,34] In the particular case of Tam HydS, we ruled out the possibility that this irreversibility is the consequence of slow interfacial electron transfer or results from the catalytic cycle being different in the two directions of the reaction,[31] but the relation between irreversible catalysis and the details of the catalytic cycle still needs to be established.

Here we follow up on recent advances in the kinetic modeling of bidirectional catalytic voltammetry[35–40] to propose an original point of view on the catalytic cycle of prototypical and atypical FeFe-hydrogenases. We aim at giving a full description of how the voltammogram shapes (catalytic potentials and limiting currents) depend on pH and H_2 concentration. Our analysis of the voltammetry of Cr HydA1 appears to be fully consistent with the above model 1, and gives further information about the thermodynamic properties of the reduced catalytic intermediates. The Tam HydS voltammetric data can be analyzed assuming that the same catalytic mechanism is operational, and this helps us identify variations in properties of the catalytic intermediates that make the two enzymes behave "reversibly" and "irreversibly".

Results

pH titration of Cr HydA1

We recorded Cr HydA1 FTIR spectra at different pH, from 5 to 10, at constant H_2 partial pressure (2% H_2 in N_2, P_{tot} = 1 atm), under equilibrium conditions. In this series of experiments, the enzyme was diluted from a concentrated stock solution into a buffer of the desired pH, so that the concentration of enzymes was always the same. Each experiment was performed in triplicate.

Figure 2A shows the spectral transition of Cr HydA1 from high pH (blue) to low pH (red). We have monitored the intensities of the bands of H_{ox} (1939 cm^{-1}) and $H_{red}H^+$ (1891 cm^{-1}), mostly present at low pH, and of H_{red} (1933 cm^{-1}) and $H_{sred}H^+$ (1881 cm^{-1}), mostly present at high pH.[8] The H_{hyd} state was omitted, because the corresponding band at around 1850 cm^{-1} was too small to be reliably quantified.

The sum of the intensities of the peaks corresponding to these four main states was constant across pH values (see SI fig. S1.1). We explain in SI section S1.1 how we

calculated the fractions of these species shown as a function of pH in fig. 2B, with the same color code as in fig. 1. By changing the pH at constant H_2 pressure, we also change the potential experienced by the enzyme at each pH value, as described by the Nernst equation. This allowed us to fit the model proposed in ref [8] to the data, considering two redox reactions, H_{ox}/H_{red} and $H_{red}H^+/H_{sred}H^+$, whose reduction potentials $E^0_1{}'$ and $E^0_2{}'$ depend on pH (as described in eqs 7 and 8 below), and one protonation whose acidity dissociation constant K defines the relative populations of H_{red} and $H_{red}H^+$. This model can be fitted to the fractions of H_{ox}, H_{red}, $H_{red}H^+$ and $H_{sred}H^+$ as a function of pH (black dashed lines in fig. 2B, see the equations in SI section S1.2) by adjusting 3 parameters: the alkaline limit of $E^0_1{}'$, -359 mV vs SHE, the acidic limit of $E^0_2{}'$, -405 mV, and the value of pK, 7.2. All these values are close to those previously measured from the results of spectroelectrochemical experiments.[8]
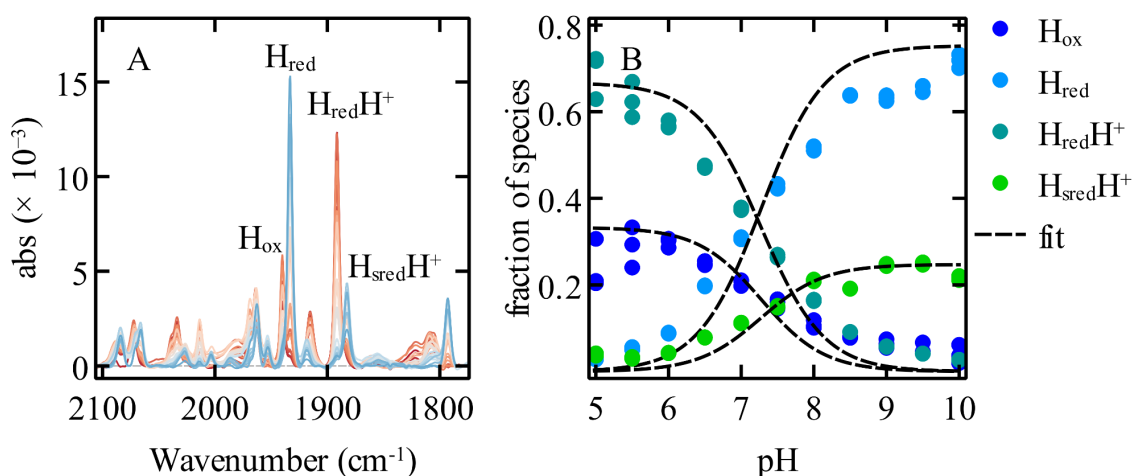

Figure 2: Cr HydA1 pH titration at 2% H_2. Panel A: overlay of the FTIR spectra baseline subtracted as a function of pH (from 5 (red) to 10 (blue)). Panel B: fit of the fraction of states H_{ox}, H_{red}, $H_{red}H^+$ and $H_{sred}H^+$ (same color code as in fig. 1) with the model proposed in ref [8] (SI section S1), giving the parameters: pK = 7.2, E^0_1 = -359 mV, E^0_2 = -405 mV vs SHE. Each data point was measured in triplicate, the dispersion of the results is visible in panel B.

These data show that very similar behavior of the Cr HydA1 enzyme is observed under thermodynamic equilibrium in a pH titration as has been observed previously in pseudo-equilibrium spectroelectrochemical titrations (ref [8]). Moreover, these data, when analyzed with an appropriate thermodynamic model, provide the relevant pKa values and redox potentials that can be compared to those derived in kinetic modeling of electrochemistry data, *vide infra*.

Further analysis of the spectroscopy of Tam HydS will be helpful to fully elucidate the relation between structures and IR signatures. In the recent, pioneering work on Tam HydS, a large hysteresis in the titration of the active site prevented the measurement of thermodynamic parameters. In combination with the limited number of H-cluster states identified in TamHydS to date, we chose not to perform the pH titration of TamHydS in this work, leaving it for future investigations.

Voltammetry

We examined the catalytic responses of Cr HydA1 and Tam HydS adsorbed onto the surface of a PGE electrode, under conditions of direct electron transfer.[33,34] We recorded cyclic voltammograms at a slow scan rate (so that the obtained current response is always under steady-state), and rotating the electrode at a fast rate so that mass transport of the substrate H_2 toward the electrode is not influential. Recording a single voltammogram gives little information about the catalytic cycle (just like the measurement of a single value of the catalytic rate in a solution assay), but we examined how the steady-state current response depends on pH at a constant H_2 pressure (1 atm.), and on the concentration of H_2 (changed by changing the partial H_2 pressure) at a constant pH (pH 6.5 for Tam HydS and 7.7 for Cr HydA1).

The steady-state catalytic responses of hydrogenases are analyzed here (and in all of our previous work) with a generic rate equation that depends on four parameters: the two limiting currents i_{lim}^{ox} and i_{lim}^{red} whose values are proportional to the turnover frequency under very oxidizing and very reducing conditions, and two "catalytic potentials", E_{cat}^{ox} and E_{cat}^{red}.[35,37,41]

$$i = \frac{i_{lim}^{ox} \exp^{F(E-E_{cat}^{ox})/RT} \exp^{F(E-E_{cat}^{red})/RT} - i_{lim}^{red}}{1 + \exp^{F(E-E_{cat}^{red})/RT}\left(1 + \exp^{F(E-E_{cat}^{ox})/RT}\right)} \quad \text{(eq 1)}$$

The catalytic potentials are the values of the electrode potential below and above which H_2 evolution and oxidation, respectively, are observed. They are measured from the positions of the inflexion potentials of the catalytic waves, or by fitting a model to the waveshape.[35,37,41] By definition, irreversible catalysis corresponds to the situation where E_{cat}^{ox} is significantly greater than E_{cat}^{red}, with a potential range where no catalysis occurs.[29–31,37]

The rate equation must be modified to account for the broadening that results from slow and distributed interfacial electron transfer, as described previously.[35,42] For this we assume that electron transfer between the electrode and the active site is direct, and that the values of the ET rate constants depend on electrode potential according to the Butler-Volmer equation. This is correct for Cr HydA1, which embeds no accessory clusters, and it is also a good approximation in the case of Tam HydS (despite the probable implication of FeS clusters in mediating long range electron transfer in this enzyme) on condition that intramolecular electron transfer is fast relative to the turn-over of Tam HydS.[35] Considering slow intramolecular electron transfer would add parameters to a model that already provides a very good fit of the data, so these parameters would necessarily be under-determined.[35]
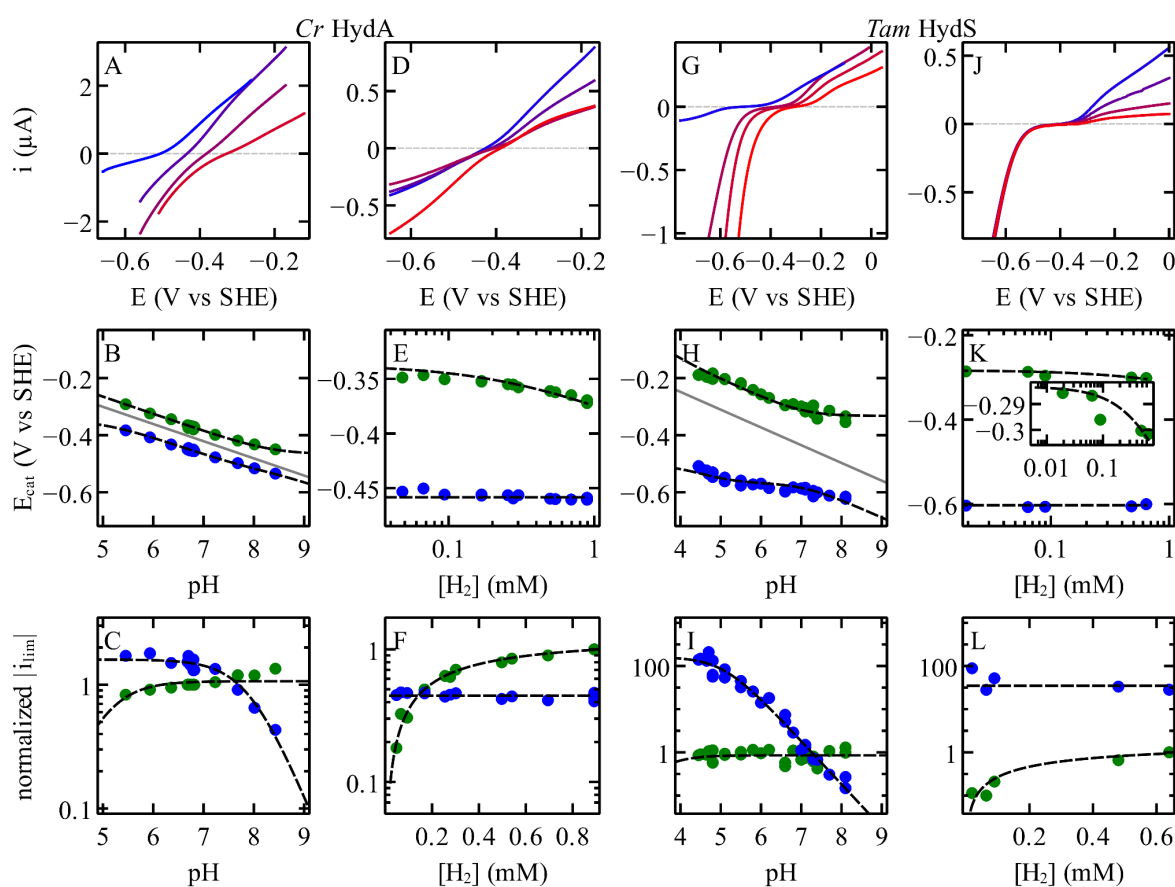
Figure 3: Cyclic voltammograms, catalytic potentials and limiting currents at different pHs and [H$_2$] pressures for Cr HydA1 and Tam HydS. The black dashed lines are the best fits of eqs 11-14, with the parameters shown in Table 1 (deduced from the analysis of the voltammetry at different pH values) or the best fits of eqs 23 and 26, with the parameters shown in table 2 (from the analysis of the voltammetry at different [H$_2$] concentrations). Panels A and D show selected blank subtracted, averaged, cyclic voltammograms for Cr HydA1 at different pH (under 1 atm. of [H$_2$], 30°C) and [H$_2$] pressures (at pH 7.7, 5°C), respectively. Colors go from blue to red from high to low pH (pH values are 5.4, 6.3, 7.2, 8.4 in panel A) and from high to low H$_2$ partial pressure (0.89, 0.36, 0.18, 0.04 mM [H$_2$] in panel D). Other conditions: scan rate 20 mV/s, electrode rotation rate 3000 rpm. Panels G and J show selected, blank subtracted, averaged cyclic voltammograms for Tam HydS at different pH (under 1 atm. of [H$_2$], 40°C) and [H$_2$] pressures (at pH 6.5, 40°C), respectively. Colors go from blue to red from high to low pH (pH values are 4.8, 5.5, 6, 8.1 in panel G) and from high to low H$_2$ partial pressure (0.64, 0.5, 0.09, 0.06 mM [H$_2$] in panel J). Other conditions: 10 mV/s, 3000 rpm. The catalytic potentials and the normalized limiting currents are plotted as a function of pH (panels B and C for Cr HydA1 and panels H and I for Tam HydS) and as a function of H$_2$ concentration (panels E and F for Cr HydA1 and panels K and L for Tam HydS). The current values were normalized by the value of i_{lim}^{ox} at pH 7 in the plots of i_{lim} against pH, and by the value of i_{lim}^{ox} under 1 atm. of H$_2$ in the plots of i_{lim} against [H$_2$]. In green E_{cat}^{ox} and i_{lim}^{ox}, in blue E_{cat}^{red} and i_{lim}^{red}. In panels B and H a solid gray line indicates the Nernst potential of the H$^+$/H$_2$ couple.

The model was then fitted to the voltammograms (see SI sections S2.7 to S2.9 and ref [31]) to measure the catalytic potentials and the high and low potential limiting currents. The latter

are related to the equilibrium potential (the Nernst potential of the H^+/H_2 couple) by the following equation:[37]

$$\frac{i_{\text{lim}}^{\text{ox}}}{i_{\text{lim}}^{\text{red}}} = \exp\left[\frac{2F}{RT}\left(\frac{E_{\text{cat}}^{\text{ox}} + E_{\text{cat}}^{\text{red}}}{2} - E_{\text{eq}}\right)\right] \quad \text{(eq 2)}$$

The steady-state rate equation (eq 1) and the constraint in eq 2 are valid for the steady-state voltammetric response of any two-electron bidirectional catalytic cycle that is "ordered" (meaning that it involves the same series of steps for the forward and backward the reactions).[37] Since the rate equation does not depend on the details of the catalytic cycle such as the order of the catalytic steps, the only conclusion from the observation that the equation fits well the voltammetry is that the catalytic mechanism is ordered. However, important insights come from the detailed interpretation of how the four parameters (catalytic potentials and limiting currents) depend on the experimental parameters, in particular pH and H_2 concentration, as discussed in ref [40] and illustrated below.

Modelling

The meaning of the catalytic potentials depends on the order and the rate constants of the steps in the catalytic cycle,[37] and to interpret the dependence of the catalytic potentials and limiting currents on pH and H_2 concentration, one has to make explicit assumptions about which rate constants depend on pH and $[H_2]$.[40] A kinetic model that would involve all the steps that have been postulated in the catalytic cycle of FeFe-hydrogenases would depend on too many parameters and would be impractical from the point of view of the kinetic analysis. Like in a recent study of H^+/H_2 conversion by a synthetic complex,[39] the compromise that we found useful was to consider a catalytic cycle model that includes four distinct steps: two redox steps ("E") and two non-redox steps ("C" for "chemical"), as depicted in fig. 4A.
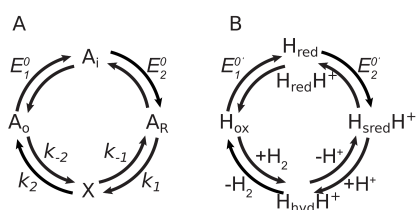

Figure 4. The kinetic schemes discussed in this paper. Panel A: The generic scheme of the catalytic mechanism EECC[1], where A is the active site (in the redox states O, oxidized, I, intermediate and R,reduced), "X" is a catalytic intermediate and all steps are reversible. Panel B: the mechanism adapted to analyze the steady-state kinetics of hydrogenases. The two electron reduction of H_{ox} to $H_{\text{sred}}H^+$ is coupled to one protonation (hence the pH dependence of E^0_1' and E^0_2' in eqs 7-8), and the 1st and 2nd chemical steps correspond to protonation (eqs 9-10) and H_2 release/binding (eqs 21-22), so that the "X" intermediate corresponds to $H_{\text{hyd}}H^+$ and $H_{\text{ox}}H_2$. Only the former is shown in panel B.

The limiting currents and catalytic potentials depend on the values of E^0_1, E^0_2 and on the values of the four rate constants of the two chemical steps, as demonstrated in ref [37]:

$$i_{\text{lim}}^{\text{ox}} = 2FA\Gamma \frac{k_{-1}k_{-2}}{k_2 + k_{-1} + k_{-2}} \quad \text{(eq 3)}$$

$$i_{\text{lim}}^{\text{red}} = -2FA\Gamma \frac{k_1 k_2}{k_1 + k_2 + k_{-1}} \quad \text{(eq 4)}$$

$$E_{\text{cat}}^{\text{ox}} = E_1^0 - \frac{RT}{F} \ln \frac{k_2 + k_{-1} + k_{-2}}{k_2 + k_{-1}} \quad \text{(eq 5)}$$

$$E_{\text{cat}}^{\text{red}} = E_2^0 + \frac{RT}{F} \ln \frac{k_2 + k_{-1} + k_1}{k_2 + k_{-1}} \quad \text{(eq 6)}$$

To match the mechanism of model 1 and the Pourbaix diagram in fig. 1C, we assume that the 1st redox step (the reduction of H_{ox}) is coupled to a fast protonation at pH < pK, so that its redox potential depends on pH according to:

$$E_1^{0\prime} = E_1^0 + \frac{RT}{F} \ln \left[1 + \frac{[H^+]}{K} \right] \quad \text{(eq 7)}$$

Where pK is the pKa of H_{red} (corresponding to the protonation of the amine bridge), and E_1^0 is the reduction potential of the H_{ox}/H_{red} couple in the alkaline limit, as indicated in fig. 1C. As a consequence, the redox potential of the second redox step is

$$E_2^{0\prime} = E_2^0 - \frac{RT}{F} \ln \left[1 + \frac{K}{[H^+]} \right] \quad \text{(eq 8)}$$

Where E_2^0 is the reduction potential of the $H_{red}H^+/H_{sred}H^+$ couple in the acidic limit. These two redox steps correspond to the two-electron one-proton reduction of H_{ox} into $H_{sred}H^+$ (fig. 1A).

The reductive catalytic cycle is completed by a series of chemical steps that include the 2nd protonation, and H_2 binding and release, which we describe in the model by two distinct, bidirectional, non-redox steps "C" (fig. 4A).

A strong assumption above is that the $H_{red}/H_{red}H^+$ transition is fast on the turnover time scale and remains at equilibrium during the catalytic cycle, whereas the second protonation is allowed to be slow. This reduces the catalytic cycle to just four steps. This approximation is given justification by the very good agreement between the resulting "EECC" model in fig. 4A and the data, as described below. Making the first protonation also slow (in what would become an "ECECC" scheme) would add parameters to a model that is already very good, so these parameters would necessarily be underdetermined (the situation is the same as that discussed above, regarding our rudimentary description of the electron transfer kinetics). In our attempts to find the "best" and simplest model, we have also considered an ECEC catalytic cycle, which failed to reproduce the pH dependence (cf SI section S2.10).

pH dependence of the Cr HydA1 voltammetric response

We first focus on the pH dependence of the catalytic potentials and limiting currents of Cr HydA1. For this we explicitly include a protonation in the 1st chemical step as shown in fig. 4B, using a realistic description of the (de)protonation kinetics (we also tested protonation in step 2, but this leads to inconsistencies, cf SI section S2.1). Since the proton is transferred to the H-cluster from the final proton relay (the side chain of a conserved cysteine residue in group A hydrogenases) rather than directly from bulk water or from the

buffer, the rate constants of the protonation and deprotonation steps, k_1 and k_{-1} respectively, depend on the pH according to :

$$k_1 = \frac{k_1^{\mathrm{max}}}{1 + \frac{K_{\mathrm{relay}}}{[\mathrm{H^+}]}} \quad \text{(eq 9)}$$

$$k_{-1} = \frac{k_{-1}^{\mathrm{max}}}{1 + \frac{[\mathrm{H^+}]}{K_{\mathrm{relay}}}} \quad \text{(eq 10)}$$

where K_{relay} is the acidity constant of the proton relay.[39,43]

Replacing $E^0{}_1$ and $E^0{}_2$ with $E^0{}_1{}'$ and $E^0{}_2{}'$ and substituting eqs 9-10 into eqs 3-6 gives the pH dependence of the two limiting currents and the two catalytic potentials as a function of 8 parameters: K, defined in eqs 7-8, $E^0{}_2$, defined above, and α, β, $E^0{}_1{}^{\mathrm{app}}$, K_1, K_2 and K_3, all defined below.

$$\mathrm{i}_{\mathrm{lim}}^{\mathrm{ox}} = \frac{\alpha}{1 + \frac{[\mathrm{H^+}]}{K_1}} \quad \text{(eq 11)}$$

$$\mathrm{i}_{\mathrm{lim}}^{\mathrm{red}} = \frac{\beta}{1 + \frac{K_3}{[\mathrm{H^+}]}} \quad \text{(eq 12)}$$

$$\mathrm{E}_{\mathrm{cat}}^{\mathrm{ox}} = \mathrm{E}_1^{0\mathrm{app}} + \frac{RT}{F} \ln\left[1 + \frac{[\mathrm{H^+}]}{K}\right] + \frac{RT}{F} \ln\left[\frac{1 + \frac{[\mathrm{H^+}]}{K_2}}{1 + \frac{[\mathrm{H^+}]}{K_1}}\right] \quad \text{(eq 13)}$$

$$\mathrm{E}_{\mathrm{cat}}^{\mathrm{red}} = \mathrm{E}_2^0 - \frac{RT}{F} \ln\left[1 + \frac{K}{[\mathrm{H^+}]}\right] + \frac{RT}{F} \ln\left[\frac{1 + \frac{[\mathrm{H^+}]}{K_3}}{1 + \frac{[\mathrm{H^+}]}{K_2}}\right] \quad \text{(eq 14)}$$

The parameters α and β in eqs 11 and 12 are pH independent:

$$\alpha = 2FA\Gamma \frac{k_{-2}k_{-1}^{\mathrm{max}}}{k_2 + k_{-2} + k_{-1}^{\mathrm{max}}} \quad \text{(eq 15)}$$

$$\beta = -2FA\Gamma \frac{k_2 k_1^{\mathrm{max}}}{k_2 + k_1^{\mathrm{max}}} \quad \text{(eq 16)}$$

They are not discussed further because their value defines the magnitude of the voltammetric current, which, in Protein Film Electrochemistry, is proportional to the unknown electroactive coverage Γ and thus cannot be interpreted.[33,44] Four of the six parameters in eqs 11-14 are related to the parameters of the catalytic cycle by the following relations:

$$\mathrm{E}_1^{0\mathrm{app}} = \mathrm{E}_1^0 + \frac{RT}{F} \ln\left[\frac{k_2 + k_{-1}^{\mathrm{max}}}{k_2 + k_{-2} + k_{-1}^{\mathrm{max}}}\right] \quad \text{(eq 17)}$$

$$K_1 = K_{\mathrm{relay}} \times \frac{k_2 + k_{-2} + k_{-1}^{\mathrm{max}}}{k_2 + k_{-2}} \quad \text{(eq 18)}$$

$$K_2 = K_{relay} \times \frac{k_2 + k_{-1}^{\mathrm{max}}}{k_2} \quad \text{(eq 19)}$$

$$K_3 = K_{relay} \times \frac{k_2 + k_{-1}^{\mathrm{max}}}{k_2 + k_1^{\mathrm{max}}} \quad \text{(eq 20)}$$

pK_1, pK_2 and pK_3 are "catalytic pKa's",[40] which depend on the acidity of the proton relay and on kinetic parameters. These apparent pKa's defined by eqs 18-20 are not thermodynamic quantities (as explained in ref [40]). They do not each correspond to the protonation of a particular intermediate, but they are three because a model that includes three protonation events (here, two at the active site and one at the proton relay) should depend on at most three apparent pKa's. Similarly, the value of $E^0_1{}^{app}$ cannot be easily interpreted because it is shifted from E^0_1, the alkaline limit of $E^0_1{}'$ (cf eq. 17). The other two parameters, E^0_2 and K, are thermodynamic quantities. We used eqs 11-14 to interpret the variations with pH of the catalytic potentials and limiting currents of Cr HydA1 (panels B, C, E and F in fig. 3).

Considering eq. 11, the observation that $i_{lim}{}^{ox}$ is pH independent (green data points in fig. 3C) implies $pK_1 < 5$. The value of $pK_3 \approx 7.9$ could be directly deduced by fitting eq 12 to the pH dependence of $i_{lim}{}^{red}$ (blue in fig. 3C).

The same apparent acidity constants ("K_i") appear in several of the equations 11-14, meaning that the four variations with pH are not independent of one another. Moreover, eqs 18-20 imply that pK_2 is necessarily lower than both pK_1 and pK_3. This gave useful constraints to interpret the pH-dependence of the catalytic potentials.

Fitting eq 14 to the pH dependence of $E_{cat}{}^{red}$ (green in fig. 3B), using the constraint $pK_2 < pK_3$ and $pK_3 \approx 7.9$ (measured from $i_{lim}{}^{ox}$) gave $E^0_2 = -523$ mV and pK = 8.3 (slightly above the value, 7.2, determined from the data in fig. 2).

Fitting eq 13 to the pH dependence of $E_{cat}{}^{ox}$ (blue in fig. 3B) with the constraint $pK_2 < pK_1$ (compare eqs 18 and 19), with pK = 8.3 (from the above fit of the pH dependence of $E_{cat}{}^{red}$), and $pK_1 < 5$ (from the pH dependence of $i_{lim}{}^{ox}$) returned $E^0_1{}^{app}$ (which is lower than $E^0_1{}'$, cf eq 17). Although it is difficult to estimate an error on the value of pK, we observed that a value of pK = 7.8 (instead of the best value 8.3) also gives a fit that is acceptable, with a value of $E^0_1{}^{app}$ that is 30 mV more positive than its best value.

These Cr HydA1 parameters are collected on the 1st row of Table 1. The values of some of the parameters can only be specified as an upper limit (e.g. $pK_1 < 5$) because any value lower than that indicated gives an equally good fit of the data.

	$E^0_1{}^{app}$ (mV)	E^0_2 (mV)	pK	pK_1	pK_2	pK_3
Cr HydA1	-466	-523	8.3	< 5	< 5	7.9
Tam HydS	-332	-568	7.1	< 3.5	< 4	5.1

Table 1: Parameters obtained by fitting eqs 11-14 to the data shown in fig. 3, to interpret the pH-dependence of the catalytic potentials and limiting currents. $E^0_1{}^{app}$ is distinct from E^0_1 (cf eq. 17).

Dependence on H_2 concentration of the Cr HydA1 voltammetric response

To explain the dependence of the catalytic potentials and limiting currents on [H_2] at constant pH, we included the binding and release of H_2 in step 2, fig. 4B, assuming for simplicity that the release of H_2 is unimolecular

$$k_2 = \mathrm{cst} \text{ (eq 21)}$$

and H_2 binding is bimolecular

$$k_{-2} = k'_{-2} \times [\mathrm{H_2}] \text{ (eq 22)}$$

Considering more complex H_2-binding kinetics (as described in SI section S2.3) is not useful: it accounts for the slight inhibition by H_2 of H_2 evolution, but it does not change the conclusions of this work, while adding to the model parameters that cannot be determined.

Substituting eqs 21-22 in eqs 3-6 gave

$$\mathrm{i_{lim}^{ox}} = 2FA\Gamma \frac{k_{-1}}{1 + \frac{K_M}{[\mathrm{H_2}]}} \text{ (eq 23)}$$

$$\mathrm{i_{lim}^{red}} = -2FA\Gamma \frac{k_1 k_2}{k_1 + k_2 + k_{-1}} \text{ (eq 24)}$$

$$\mathrm{E_{cat}^{ox}} = \mathrm{E_1^{0'}} - \frac{RT}{F} \ln\left[1 + \frac{[\mathrm{H_2}]}{K_M}\right] \text{ (eq 25)}$$

$$\mathrm{E_{cat}^{red}} = \mathrm{E_2^{0app}} = \mathrm{E_2^{0'}} + \frac{RT}{F} \ln \frac{k_2 + k_{-1} + k_1}{k_2 + k_{-1}} \text{ (eq 26)}$$

with

$$K_M = \frac{k_2 + k_{-1}}{k'_{-2}} \text{ (eq 27)}$$

We fitted eqs 23-27 to interpret the dependence of the limiting currents and catalytic potentials recorded at constant pH on H_2 concentration.

The reductive limiting current is nearly independent of H_2 (blue in fig. 3F), consistent with eq. 24. The change in $\mathrm{i_{ox}^{lim}}$ against $[\mathrm{H_2}]$ (green in fig. 3F, and eq. 23) returned a value of K_M = 0.3 mM that is consistent with previous measurements of ours[45].

Equation 26 is consistent with the observation that $\mathrm{E_{cat}^{red}}$ is independent of H_2 pressure. Fitting a horizontal line to $\mathrm{E_{cat}^{red}}$ (blue in fig. 3E) gave the value of $\mathrm{E_2^{0app}}$ reported in Table 2, which is offset from the value of $\mathrm{E_2^{0'}}$ (cf eq. 26).

Equation 25 accounts for the observed decrease in E_{cat}^{ox} as the concentration of H_2 increases above the value of K_M (green in in fig. 3E). The effect is small because the value of K_M is high (even at the low temperature, 5°C, that we used in this series of experiments) and it is not possible to record data at H_2 concentrations well above K_M. Yet the trends are clear and fully consistent with eqs 23-27.

	$E_1^{0'}$ (mV)	E_2^{0app} (mV)	K_M (mM)
Cr HydA1	-337	-458	0.3
Tam HydS	-283	-603	0.6

Table 2: Parameters obtained by fitting eqs 23-27 to the data shown in panels E,F, K and L of fig. 3, to interpret the dependence on $[\mathrm{H_2}]$ of the catalytic potentials and limiting currents at pH = 7.7 (Cr HydA1) and 6.5 (Tam HydS). The corresponding Cr HydA1 data (fig. 3E and F) were recorded at 5°C, where the K_M is lower [45] and the variations of E_{cat}^{ox} and $\mathrm{i_{lim}^{ox}}$ against H_2 more clearly seen. Here the value of the parameter $\mathrm{E_2^{0app}}$ is offset from $\mathrm{E_2^{0'}}$ (cf eq. 26) and thus cannot be interpreted.

Analysis of the Tam data

We used the same kinetic model, the same assumptions and the same approach to analyse the "irreversible" voltammograms obtained with the enzyme from Tam HydS (panels G to L in fig. 3). The only difference was that, as explained before,[31] the equilibrium potential was measured using a platinized electrode, and its value was used to constrain the fit (using eq. 2) to obtain well-defined values of the catalytic potentials; this was not needed for the Cr HydA1 data, because the Cr HydA1 catalytic current sharply crosses the potential axis at $E=E_{eq}$.

The variations with pH and [H_2] of the limiting currents (panels I and L in fig. 3) are similar to those observed with Cr HydA1 (panels C and F).

The value of K_M is larger than that of Cr (cf table 2), but this is explained by the Tam HydS experiments being carried out at 40°C, compared to 5°C for the dependence on [H_2] of the Cr HydA1 data (a high temperature was required because the activity of Tam HydS and the catalytic currents are small), and the value of K_M increases with temperature.[45] We confirmed this K_M value at 40°C, measured from the CVs in fig. 3, by the chronoamperometry experiments shown in SI section S2.6. The large value of K_M makes the dependence of E_{cat}^{ox} on [H_2] in Tam HydS flatter than in Cr HydA1, but the increase in E_{cat}^{ox} at low H_2 concentrations is clearly observed (inset in fig. 3K), consistent with eq. 25. This cannot be explained by assuming H_2 binding in step 1 (cf SI section 2.2).

Also, the value of pK_3 is significantly lower in Tam HydS than in Cr HydA1 (cf table 1) which is seen from the saturation of the H_2 evolution current below a lower value of the pH, compare panels C and I in fig. 3. For Tam HydS, the value of pK_3=5.1 measured from the pH dependence of i_{lim}^{red} (blue in fig. 3I) is also clearly seen as an inflexion in the pH dependence of E_{cat}^{red} (green in fig. 3H). The larger difference between pK and pK_3 in Tam HydS compared to Cr HydA1 (still with values of pK_1 and pK_2 outside the experimental pH range) explains the non-linear pH-dependence of the catalytic potentials seen in fig. 3H.

The K_M value measured here for Tam HydS is close to that measured for other FeFe-hydrogenase, despite the putative implication of Tam HydS in sensing rather than catalysis. That the Michaelis constants of FeFe-hydrogenases are apparently all similar contrasts with the situation observed with other series of homologous enzymes: the K_M values of CO-dehydrogenases for example range over orders of magnitude[46]. But a Michaelis constant is a convoluted kinetic parameter (eq 27) whose meaning is not straightforward.

Discussion

Protein film voltammetry gives the dependence of activity on electrochemical driving force, from which "catalytic potentials" can be measured.[37,41] In the case of H^+/H_2 conversion by hydrogenases, these are the values of the electrode potentials below which and above which H_2 evolution and oxidation, respectively, are observed. How these values depend on substrate concentration can be interpreted to learn about the sequence of events in the catalytic cycle,[33,47,48] but in the particular case of hydrogenases, that the protonation steps may be slow in the timescale of turnover significantly complicates their interpretation: the catalytic potentials depart from the equilibrium reduction potentials measured in redox titrations.

The catalytic potentials can be measured without making any assumption about the catalytic cycle, but their values depart from the true (equilibrium) reduction potentials of the active site, and their meaning depends on the details of the catalytic cycle. Similarly, we have shown before that if protonation is slow on the time scale of turnover, the dependence of the catalytic potentials and limiting currents on pH defines apparent pKa's, which we called "catalytic pKa's". These pKa's are kinetic parameters whose interpretation is model dependent[40]. That a catalytic system under steady-state turnover conditions defines apparent parameters (apparent potentials, acidity or dissociation constants) is not unexpected: it is textbook knowledge that a Michaelis-Menten constant is an apparent dissociation constant that depends on all steps in the catalytic cycle, rather than a true thermodynamic parameter.

Here we interpreted and compared the variations with pH and H_2 pressure of the catalytic potentials and limiting currents of the "reversible" hydrogenases Cr HydA1 and the "irreversible" one Tam HydS using a kinetic model of catalysis based on the current knowledge of the catalytic cycle (model 1 in fig. 1D). According to this model, the most oxidized H_{ox} state is reduced in two one-electron transfer steps, one of which is coupled to protonation, and the resulting $H_{sred}H^+$ species undergoes protonation before it releases H_2. Model 2 could not be used to analyze the voltammetric data, because the transition from H_{red}' to the low pH inactive branch (H_{red}, and H_{sred} in fig. 1E), and from $H_{ox}H$ to the presumably less active H_{ox} state at high pH should induce a decrease in proton reduction activity as the pH is lowered, and a decrease in H_2 oxidation activity as the pH is increased, neither of which are observed under conditions of direct electron transfer (panels C and I in fig. 3). The pH-independent, slow formation of reduced inactive states has been observed in FeFe-hydrogenases, under conditions that are more reducing than those used in this work, but they have not been associated with specific spectroscopic signatures.[49,50]

Interpreting the kinetics of the catalytic cycle in the context of model 1 implies the pH dependences of the reduction potentials of the two ET steps given by eqs 7 and 8, and the dependence on pH and H_2 concentration of the two non-redox steps given by eqs 9-10 and 21-22, respectively. Substitution in eqs 3-6 gave the relations 11-14 and 23-26, which successfully predict the variations in limiting currents and catalytic potentials as a function of pH at constant H_2 pressure, and as a function of H_2 at constant pH.

In contrast, considering either the protonation in step 2 or H_2 release in step 1 does not give a consistent description of the data. With this hypothesis, equations 11-14 remain valid, but the meaning of the catalytic pKs and the constraints differ (cf SI section S2.1). Fitting this model to the pH variations of E_{cat} and i_{lim} of Cr HydA1 and Tam HydS returns pK < 5 and pK < 4, respectively. This is not consistent with the value of pK= 7.2 measured in Cr HydA1[8]. A low value of pK is expected if we consider the catalytic cycle of model 2 (without the inactive states, that is $H_{ox}H \rightarrow$ unprotonated $H_{red}' \rightarrow H_{hyd} \rightarrow H_{ox}H$, solid arrows in fig. 1E) ; this mechanistic hypothesis may explain the observed dependence on pH of the Cr HydA1 data on condition that H_2 release is in step 1, and protonation in step 2, but then this models predicts the wrong variation of E_{cat}^{ox} with $[H_2]$ (SI section S2.2). Therefore, we have not been able to reconcile model 2 with the Cr HydA1 data.

For the same reasons, the analysis of the Tam HydS voltammetry gives a pK value for the half-reduced state close to 7. This is not consistent with the spectroscopic investigation of Tm HydS, which did not detect any protonated state of the H-cluster.[24] This will have to be

investigated further by examining how the reduction potentials of the active sites of Tm and Tam HydS depend on pH, which is probably the easiest way to detect the coupling between protonation and reduction which is assumed in our kinetic model and which necessarily occurs in the catalytic cycle of hydrogenases.

Regarding the analysis of the Cr HydA1 data, the parameters that we deduced by fitting eqs 11-14 and 23-26 (tables 1 and 2, respectively) are consistent with the results of previous investigations: the pKa of the one-electron reduced state (pK ≈ 8.3) is close enough to that measured in redox titrations (7.2 in ref [8]) and pH titrations (pK around 7.5 in fig. 5C of ref [9], and 7.2 from the data in fig. 2) ; the value of K_M also matches previous chronoamperometric measurements.[45] It is not possible to deduce the alkaline limit E^0_1 from the analysis of the pH dependence of the catalytic potentials, because it is shifted from the value of the parameter that we can measure, $E^0_1{}^{app}$, cf eq. 17. However, the analysis of the dependence on H_2 concentration at constant pH gives the value of $E^0_1{}'$ at pH=7.7, -337 mV, which matches the value of -362 mV at pH 8 in ref [8] (this value is confirmed from the analysis of the data in fig. 2). The acidic limit of $E^0_2{}'$ obtained from the analysis of the voltammetry at different pH values (E^0_2 = -523 mV at 30°C, table 1) is lower than the value of -417 mV at 15°C measured in ref [8] and -405 mV at room temperature from the equilibrium FTIR data in fig. 2. However, the reduction potentials are temperature dependent, and the analysis of the pH-dependence of the voltammetry at 5°C gives E^0_2 = -457 mV (SI section S2.5), which we consider close enough to the results of the spectroscopic titrations.
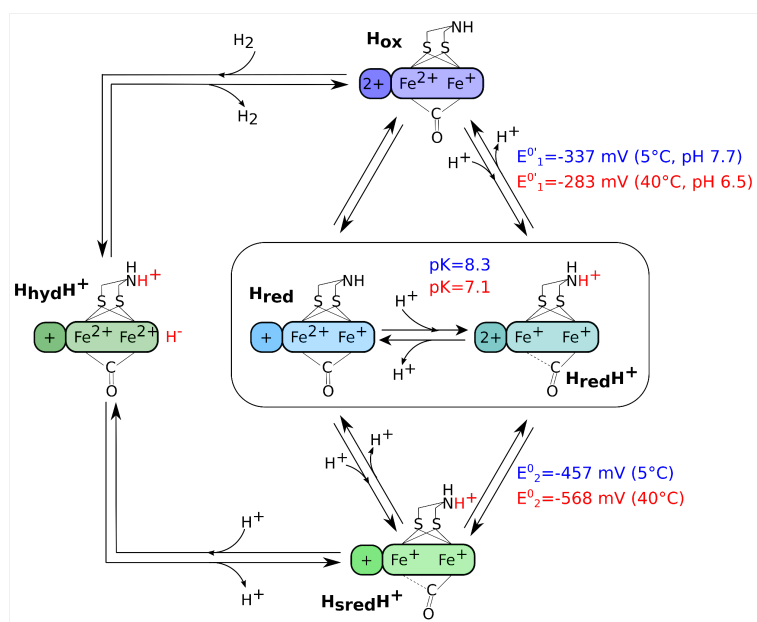

Figure 5: Proposed catalytic cycle for FeFe-hydrogenases. The intermediate states of the catalytic cycle are colored as in fig. 1. The values of $E^0_1{}'$, E^0_2 and pK obtained by fitting the voltammetry of Cr HydA1 and Tam HydS at different pH values and H_2 partial pressures are marked on the right of the figure in blue and red, respectively. The values of $E^0_1{}'$ were obtained by the analysis at different H_2 pressures, at a specific pH, reported in the figure. E^0_2 is measured from the analysis at different pHs, and it is the acidic limit of $E^0_2{}'$, independent of pH when pH<pK. In the kinetic model, the $H_{red}/H_{red}H^+$ transition (inside the rectangle) is assumed to remain in equilibrium.

Regarding Tam HydS, there are no available results of equilibrium titrations that we could compare to the values of E^0_2 in table 1 and $E^0_1{}'$ in table 2, since the titration in fig. S8 of ref [25] shows a very strong hysteresis that attests to a strong departure from equilibrium. However, the titration of Tm HydS in ref [24] is consistent with the larger thermodynamic stability of $H_{red}/H_{red}H^+$ that we detect in Tam HydS: the result of the titration gave $E^0_1{}' = -300$ and $E^0_2{}' = -570$ mV in Tm HydS at pH 8 [24], while the analysis of the voltammetry of Tam HydS returns $E^0_1{}' = -283$ at pH 6.5 (table 2), and E^0_2 (the acidic limit of $E^0_2{}'$) = -568 mV (table 1).

We assumed that the same mechanism applies in Cr HydA1 and Tam HydS (Fig. 5), but their catalytic waveshapes are different, and so are the parameters that we measured from the analyses of the variations with pH and H_2 of their catalytic potentials and limiting currents. These differences between Cr HydA1 and Tam HydS are all consistent with an increased irreversibility of the catalytic response in Tam HydS compared to Cr HydA1 (i.e. a larger separation between the oxidative and reductive catalytic potentials).

Our data show that the half-reduced catalytic intermediate (considering both H_{red} and $H_{red}H^+$) is stable over a range of potential that is about 165 mV larger in Tam HydS than in Cr HydA1, which results from both E^0_1 being more positive in Tam HydS than in Cr HydA1, and E^0_2 being more negative (tables 2 and 1, respectively). This thermodynamic stability of the half-reduced state contributes to make the catalytic response of Tam HydS very irreversible.

In contrast, the unstable nature of the half-reduced active site is a key feature of bidirectional reversible catalysts.[32,37] The difference $E^0_1{}' - E^0_2{}'$ is indeed less positive in Cr HydA1 than in Tam HydS, and even negative in the case of two recently described bidirectional reversible synthetic catalysts. The +1 redox state of the $[Pt(depe)_2][PF_6]_2$ (depe = 1,2-bis(diethylphosphino)ethane) complex that converts CO_2 and formate in acetonitrile is inherently unstable, and the reduction of $[Pt(depe)_2]^{2+}$ is therefore a cooperative two-electron process.[51,52] The recent investigation of the $[Ni(P_2{}^{Cy}N_2{}^{Arg})_2]^{6+}$ Dubois complex that reversibly converts H^+ and H_2[30,53] also showed that the reduction potential of the $Ni^{II}/Ni^{I}H^+$ couple is much lower than that of the more reduced $Ni^{III}H^-/Ni^{II}H^-$ couple, which makes the half-reduced tautomers $Ni^{I}H^+$ and $Ni^{III}H^-$ unstable.[39] In both cases therefore, potential inversion[54] destabilizes the half-reduced form of the active site, and thus decreases $E_{cat}{}^{ox}-E_{cat}{}^{red}$ and contributes to make the response reversible.

Another difference between the two hydrogenases is seen as a lower value of pK_3 in Tam HydS compared to Cr HydA1 (table 1), which contributes to decrease $E_{cat}{}^{red}$ (cf eq. 14). Considering the definition of K_3 in eq. 20, the lower value of pK_3 can be interpreted in two different manners. One explanation is that the proton transfer relay has lower pKa (the acidity constant is "K_{relay}" in eqs 18-20), which is consistent with the recent finding that the proton donor to the active site is the side chain of a glutamate residue in Tam HydS,[27] compared to a cysteine residue in Cr HydA1 and other prototypical hydrogenases.[3] The other explanation applies if the rate constant of H_2 binding at the active site is smaller than the (de)protonation rate constants. In that case, K_3 equates $k_{-1}{}^{max}/k_1{}^{max} K_{relay}$, which is the acidity constant of the doubly reduced catalytic intermediate (cf SI section S2.4), and our analysis suggests that this intermediate is harder to protonate in Tam HydS than in Cr HydA1. This protonation, which is required to close the catalytic cycle, has so far proven challenging to firmly identify in spectroscopic investigations.[16,19]

Overall, our results point to various functional differences between Cr HydA1 and Tam HydS, which all contribute to make the catalytic response of the former more reversible: the lower

stability of the half-reduced state (smaller difference between $E^0_1{}'$ and $E^0_2{}'$, which has not been rationalized yet in terms of active site proteic environment [28]), and the easier protonation of the relay or of the two-electron reduced state (larger pK_3).

We conclude on the consideration, which is clear from eq 25, on the role played by the stabilization of the enzyme-substrate complex ($H_{hyd}H^+$) is decreasing the oxidative catalytic potential, and therefore increasing the reversibility of the catalytic signal. An experimental comparison between Cr HydA1 and Tam HydS in this respect is difficult, because the Michaelis constants are difficult to measure accurately, and impossible to measure and compare at the same temperature. However, eq 25 is another illustration of the idea that flat energy landscapes are not required to obtain a reversible catalytic response [37,39]: that the catalytic cycle includes high or low energy intermediates may favor reversibility, sometimes at the expense of turnover frequency.

Methods

The samples of Cr HydA1 and Tam HydS were produced by heterologous expression in *Escherichia coli* followed by artificial maturation with $[2Fe]^{adt}$ cofactor as described in refs with minor modifications (for details see SI) [25,55,56].

The FTIR measurements were performed in a home built cell in which a sample of 12 µL of 0.3 mM of Cr HydA1 in mixed buffer (20 mM each of acetate, MES, HEPES, Tris, glycine, CAPS) prepared under a 2% H2/98% N2 atmosphere in an anaerobic chamber (Coy) was closed between two CaF_2 windows separated by a 50 µm Teflon spacer. The sample so composed was sealed into the home built cell with two rubber rings separating the windows from the rest of the housing. The data were recorded in a standard transmission IR spectrometer (a Bruker Vertex v80) equipped with a liquid nitrogen cooled mercury-cadmium-telluride (MCT) detector.

All the electrochemistry experiments were carried out in a Jacomex glove box filled with nitrogen. The 3-electrodes electrochemical setup was described in ref [57]. The electrochemical cell solution was continuously flushed with either pure H_2 or with a mixture of H_2 and Ar adjusted to the desired composition using mass flow controllers (SLA5850S from BROOKS Instruments). The resulting H_2 concentration was calculated from the H_2 partial pressure assuming a solubility of 0.89 mM/atm at 5°C and 0.64 mM/atm at 40°C.[58,59]

The films of Cr HydA1 on PGE electrodes were prepared by letting adsorb 0.5 µL of enzyme solution (5-20 µM) for about 3 minutes, after having polished the electrode surface (~0.1 cm^2) with 1 µm aqueous alumina slurry. The films of Tam HydS were prepared by polishing the electrode surface with 1 µm aqueous alumina slurry and P1200 sandpaper. After sonication, 1 µL of enzyme solution (5-10 µM) was painted on the electrode surface together with 1 µL of polymyxin B sulphate (2-20 mg/mL), and let dry for 5 to 10 minutes. The platinized electrode to measure the H^+/H_2 equilibrium potential during the Tam HydS experiments was prepared according to the protocol in ref [60].

All the electrochemical experiments were performed in a chloride free mixed buffer: MES, CHES, HEPES, TAPS, Na acetate (all 5 mM), and Na_2SO_4 (0.1 M).

All potentials were measured with respect to a saturated calomel electrode and then corrected to the SHE by using $E_{SHE} = E_{SCE} + 241$ mV.

We accounted for film loss during the series of voltammograms by always recording one CV at pH 7 or at 1 mM [H_2] between every experiment at a different pH or H_2 pressure, respectively, and normalizing the limiting currents (as e.g. in ref [61]). Only in the series of experiments with Tam HydS as a function of pH was this not necessary because the films were very stable. The capacitive current was removed by subtracting a blank recorded with no enzyme, and the forward and backward sweeps averaged.

The data were analyzed using the Qsoas software, available at www.qsoas.org.[62]

Supporting Information

Section S1: additional experimental details, materials, and methods regarding the experiment in fig. 2. Section S2: additional kinetic models and their discussions ; fits of Ecat and i_{lim} as a function of pH at 5°C for Cr HydA1 ; Tam HydS K_M measurement ; analysis of the cyclic voltammograms of Cr HydA1 and Tam HydS recorded under various conditions. Section S3. Preparation of [2Fe]ADT- activated Tam HydS. The SI file is available free of charge at https://pubs.acs.org

Acknowledgements

References

(1) Silakov, A.; Wenk, B.; Reijerse, E.; Lubitz, W. 14N HYSCORE Investigation of the H-Cluster of [FeFe] Hydrogenase: Evidence for a Nitrogen in the Dithiol Bridge. *Phys. Chem. Chem. Phys.* **2009**, *11* (31), 6592–6599. doi: 10.1039/B905841A

(2) Berggren, G.; Adamska, A.; Lambertz, C.; Simmons, T. R.; Esselborn, J.; Atta, M.; Gambarelli, S.; Mouesca, J. M.; Reijerse, E.; Lubitz, W.; Happe, T.; Artero, V.; Fontecave, M. Biomimetic Assembly and Activation of [FeFe]-Hydrogenases. *Nature* **2013**, *499* (7456), 66–69. doi: 10.1038/nature12239

(3) Duan, J.; Senger, M.; Esselborn, J.; Engelbrecht, V.; Wittkamp, F.; Apfel, U.-P.; Hofmann, E.; Stripp, S. T.; Happe, T.; Winkler, M. Crystallographic and Spectroscopic Assignment of the Proton Transfer Pathway in [FeFe]-Hydrogenases. *Nat. Commun.* **2018**, *9* (1), 4726. doi: 10.1038/s41467-018-07140-x

(4) Cornish, A. J.; Gärtner, K.; Yang, H.; Peters, J. W.; Hegg, E. L. Mechanism of Proton Transfer in [FeFe]-Hydrogenase from Clostridium Pasteurianum. *J. Biol. Chem.* **2011**, *286* (44), 38341–38347. doi: 10.1074/jbc.M111.254664

(5) Greening, C.; Biswas, A.; Carere, C. R.; Jackson, C. J.; Taylor, M. C.; Stott, M. B.; Cook,

G. M.; Morales, S. E. Genomic and Metagenomic Surveys of Hydrogenase Distribution Indicate H2 Is a Widely Utilised Energy Source for Microbial Growth and Survival. *ISME J.* **2016**, *10* (3), 761–777. doi: 10.1038/ismej.2015.153

(6) Birrell, J. A.; Rodríguez-Maciá, P.; Reijerse, E. J.; Martini, M. A.; Lubitz, W. The Catalytic Cycle of [FeFe] Hydrogenase: A Tale of Two Sites. *Coord. Chem. Rev.* **2021**, *449*, 214191. doi: 10.1016/j.ccr.2021.214191

(7) Lorent, C.; Katz, S.; Duan, J.; Kulka, C. J.; Caserta, G.; Teutloff, C.; Yadav, S.; Apfel, U.-P.; Winkler, M.; Happe, T.; Horch, M.; Zebger, I. Shedding Light on Proton and Electron Dynamics in [FeFe] Hydrogenases. *J. Am. Chem. Soc.* **2020**, *142* (12), 5493–5497. doi: 10.1021/jacs.9b13075

(8) Sommer, C.; Adamska-Venkatesh, A.; Pawlak, K.; Birrell, J. A.; Rüdiger, O.; Reijerse, E. J.; Lubitz, W. Proton Coupled Electronic Rearrangement within the H-Cluster as an Essential Step in the Catalytic Cycle of [FeFe] Hydrogenases. *J. Am. Chem. Soc.* **2017**, *139* (4), 1440–1443. doi: 10.1021/jacs.6b12636

(9) Laun, K.; Baranova, I.; Duan, J.; Kertess, L.; Wittkamp, F.; Apfel, U.-P.; Happe, T.; Senger, M.; Stripp, S. T. Site-Selective Protonation of the One-Electron Reduced Cofactor in [FeFe]-Hydrogenase. *Dalton Trans.* **2021**, *50* (10), 3641–3650. doi: 10.1039/d1dt00110h

(10) Roseboom, W.; De Lacey, A. L.; Fernandez, V. M.; Hatchikian, E. C.; Albracht, S. P. J. The Active Site of the [FeFe]-Hydrogenase from Desulfovibrio Desulfuricans. II. Redox Properties, Light Sensitivity and CO-Ligand Exchange as Observed by Infrared Spectroscopy. *J. Biol. Inorg. Chem.* **2006**, *11* (1), 102–118. doi: 10.1007/s00775-005-0040-2

(11) Mebs, S.; Senger, M.; Duan, J.; Wittkamp, F.; Apfel, U.-P.; Happe, T.; Winkler, M.; Stripp, S. T.; Haumann, M. Bridging Hydride at Reduced H-Cluster Species in [FeFe]-Hydrogenases Revealed by Infrared Spectroscopy, Isotope Editing, and Quantum Chemistry. *J. Am. Chem. Soc.* **2017**, *139* (35), 12157–12160. doi: 10.1021/jacs.7b07548

(12) Ratzloff, M. W.; Artz, J. H.; Mulder, D. W.; Collins, R. T.; Furtak, T. E.; King, P. W. CO-Bridged H-Cluster Intermediates in the Catalytic Mechanism of [FeFe]-Hydrogenase CaI. *J. Am. Chem. Soc.* **2018**, *140* (24), 7623–7628. doi: 10.1021/jacs.8b03072

(13) Birrell, J. A.; Pelmenschikov, V.; Mishra, N.; Wang, H.; Yoda, Y.; Tamasaku, K.; Rauchfuss, T. B.; Cramer, S. P.; Lubitz, W.; DeBeer, S. Spectroscopic and Computational Evidence That [FeFe] Hydrogenases Operate Exclusively with CO-Bridged Intermediates. *J. Am. Chem. Soc.* **2020**, *142* (1), 222–232. doi: 10.1021/jacs.9b09745

(14) Adamska, A.; Silakov, A.; Lambertz, C.; Rüdiger, O.; Happe, T.; Reijerse, E.; Lubitz, W. Identification and Characterization of the "Super-Reduced" State of the H-Cluster in [FeFe] Hydrogenase: A New Building Block for the Catalytic Cycle? *Angew. Chem. Int. Ed Engl.* **2012**, *51* (46), 11458–11462. doi: 10.1002/anie.201204800

(15) Pelmenschikov, V.; Birrell, J. A.; Pham, C. C.; Mishra, N.; Wang, H.; Sommer, C.; Reijerse, E.; Richers, C. P.; Tamasaku, K.; Yoda, Y.; Rauchfuss, T. B.; Lubitz, W.; Cramer, S. P. Reaction Coordinate Leading to H2 Production in [FeFe]-Hydrogenase Identified by Nuclear Resonance Vibrational Spectroscopy and Density Functional Theory. *J. Am. Chem. Soc.* **2017**, *139* (46), 16894–16902. doi: 10.1021/jacs.7b09751

(16) Mulder, D. W.; Ratzloff, M. W.; Bruschi, M.; Greco, C.; Koonce, E.; Peters, J. W.; King, P. W. Investigations on the Role of Proton-Coupled Electron Transfer in Hydrogen Activation by [FeFe]-Hydrogenase. *J. Am. Chem. Soc.* **2014**, *136* (43), 15394–15402. doi: 10.1021/ja508629m

(17) Mulder, D. W.; Guo, Y.; Ratzloff, M. W.; King, P. W. Identification of a Catalytic Iron-Hydride at the H-Cluster of [FeFe]-Hydrogenase. *J. Am. Chem. Soc.* **2017**, *139* (1), 83–86. doi: 10.1021/jacs.6b11409

(18) Rumpel, S.; Sommer, C.; Reijerse, E.; Farès, C.; Lubitz, W. Direct Detection of the

Terminal Hydride Intermediate in [FeFe] Hydrogenase by NMR Spectroscopy. *J. Am. Chem. Soc.* **2018**, *140* (11), 3863–3866. doi: 10.1021/jacs.8b00459

(19)   Mészáros, L. S.; Ceccaldi, P.; Lorenzi, M.; Redman, H. J.; Pfitzner, E.; Heberle, J.; Senger, M.; Stripp, S. T.; Berggren, G. Spectroscopic Investigations under Whole-Cell Conditions Provide New Insight into the Metal Hydride Chemistry of [FeFe]-Hydrogenase. *Chem. Sci.* **2020**, *11* (18), 4608–4617. doi: 10.1039/D0SC00512F

(20)   Senger, M.; Laun, K.; Wittkamp, F.; Duan, J.; Haumann, M.; Happe, T.; Winkler, M.; Apfel, U.-P.; Stripp, S. T. Proton-Coupled Reduction of the Catalytic [4Fe-4S] Cluster in [FeFe]-Hydrogenases. *Angew. Chem. Int. Ed Engl.* **2017**, *56* (52), 16503–16506. doi: 10.1002/anie.201709910

(21)   Rodríguez-Maciá, P.; Breuer, N.; DeBeer, S.; Birrell, J. A. Insight into the Redox Behavior of the [4Fe–4S] Subcluster in [FeFe] Hydrogenases. *ACS Catal.* **2020**, *10* (21), 13084–13095. doi: 10.1021/acscatal.0c02771

(22)   Martini, M. A.; Rüdiger, O.; Breuer, N.; Nöring, B.; DeBeer, S.; Rodríguez-Maciá, P.; Birrell, J. A. The Nonphysiological Reductant Sodium Dithionite and [FeFe] Hydrogenase: Influence on the Enzyme Mechanism. *J. Am. Chem. Soc.* **2021**, *143* (43), 18159–18171. doi: 10.1021/jacs.1c07322

(23)   Senger, M.; Duan, J.; Pavliuk, M. V.; Apfel, U.-P.; Haumann, M.; Stripp, S. T. Trapping an Oxidized and Protonated Intermediate of the [FeFe]-Hydrogenase Cofactor under Mildly Reducing Conditions. *Inorg. Chem.* **2022**, *61* (26), 10036–10042. doi: 10.1021/acs.inorgchem.2c00954

(24)   Chongdar, N.; Birrell, J. A.; Pawlak, K.; Sommer, C.; Reijerse, E. J.; Rüdiger, O.; Lubitz, W.; Ogata, H. Unique Spectroscopic Properties of the H-Cluster in a Putative Sensory [FeFe] Hydrogenase. *J. Am. Chem. Soc.* **2018**, *140* (3), 1057–1068. doi: 10.1021/jacs.7b11287

(25)   Land, H.; Sekretareva, A.; Huang, P.; Redman, H. J.; Németh, B.; Polidori, N.; Mészáros, L. S.; Senger, M.; Stripp, S. T.; Berggren, G. Characterization of a Putative Sensory [FeFe]-Hydrogenase Provides New Insight into the Role of the Active Site Architecture. *Chem. Sci.* **2020**, *11* (47), 12789–12801. doi: 10.1039/d0sc03319g

(26)   Calusinska, M.; Happe, T.; Joris, B.; Wilmotte, A. The Surprising Diversity of Clostridial Hydrogenases: A Comparative Genomic Perspective. *Microbiology* **2010**, *156* (Pt 6), 1575–1588. doi: 10.1099/mic.0.032771-0

(27)   Cabotaje, P. R.; Walter, K.; Zamader, A.; Huang, P.; Ho, F.; Land, H.; Senger, M.; Berggren, G. Probing Substrate Transport Effects on Enzymatic Hydrogen Catalysis: An Alternative Proton Transfer Pathway in Putatively Sensory [FeFe] Hydrogenase. *ACS Catal.* **2023**, *13* (15), 10435–10446. doi: 10.1021/acscatal.3c02314

(28)   Chongdar, N.; Rodríguez-Maciá, P.; Reijerse, E. J.; Lubitz, W.; Ogata, H.; Birrell, J. A. Redox Tuning of the H-Cluster by Second Coordination Sphere Amino Acids in the Sensory [FeFe] Hydrogenase from Thermotoga Maritima. *Chem. Sci.* **2023**, *14* (13), 3682–3692. doi: 10.1039/d2sc06432d

(29)   Armstrong, F. A.; Hirst, J. Reversibility and Efficiency in Electrocatalytic Energy Conversion and Lessons from Enzymes. *Proc. Natl. Acad. Sci. U. S. A.* **2011**, *108* (34), 14049–14054. doi: 10.1073/pnas.1103697108

(30)   Dutta, A.; Appel, A. M.; Shaw, W. J. Designing Electrochemically Reversible H2 Oxidation and Production Catalysts. *Nature Reviews Chemistry* **2018**, *2* (9), 244–252. doi: 10.1038/s41570-018-0032-8

(31)   Fasano, A.; Land, H.; Fourmond, V.; Berggren, G.; Léger, C. Reversible or Irreversible Catalysis of H+/H2 Conversion by FeFe Hydrogenases. *J. Am. Chem. Soc.* **2021**, *143* (48), 20320–20325. doi: 10.1021/jacs.1c09554

(32)   Fourmond, V.; Plumeré, N.; Léger, C. Reversible Catalysis. *Nature Reviews Chemistry* **2021**, *5* (5), 348–360. doi: 10.1038/s41570-021-00268-3

(33)   Léger, C.; Bertrand, P. Direct Electrochemistry of Redox Enzymes as a Tool for Mechanistic Studies. *Chem. Rev.* **2008**, *108* (7), 2379–2438. doi: 10.1021/cr0680742

(34)   Sensi, M.; del Barrio, M.; Baffert, C.; Fourmond, V.; Léger, C. New Perspectives in Hydrogenase Direct Electrochemistry. *Current Opinion in Electrochemistry* **2017**, *5* (1), 135–145. doi: 10.1016/j.coelec.2017.08.005

(35)   Fourmond, V.; Baffert, C.; Sybirna, K.; Lautier, T.; Abou Hamdan, A.; Dementin, S.; Soucaille, P.; Meynial-Salles, I.; Bottin, H.; Léger, C. Steady-State Catalytic Wave-Shapes for 2-Electron Reversible Electrocatalysts and Enzymes. *J. Am. Chem. Soc.* **2013**, *135* (10), 3926–3938. doi: 10.1021/ja311607s

(36)   Savéant, J.-M. Molecular Catalysis of Electrochemical Reactions. Cyclic Voltammetry of Systems Approaching Reversibility. *ACS Catal.* **2018**, *8* (8), 7608–7611. doi: 10.1021/acscatal.8b02007

(37)   Fourmond, V.; Wiedner, E. S.; Shaw, W. J.; Léger, C. Understanding and Design of Bidirectional and Reversible Catalysts of Multielectron, Multistep Reactions. *J. Am. Chem. Soc.* **2019**, *141* (28), 11269–11285. doi: 10.1021/jacs.9b04854

(38)   Costentin, C. Molecular Catalysis of Electrochemical Reactions. Overpotential and Turnover Frequency: Unidirectional and Bidirectional Systems. *ACS Catal.* **2021**, *11* (9), 5678–5687. doi: 10.1021/acscatal.1c00744

(39)   Reuillard, B.; Costentin, C.; Artero, V. Deciphering Reversible Homogeneous Catalysis of the Electrochemical H_2 Evolution and Oxidation: Role of Proton Relays and Local Concentration Effects. *Angew. Chem. Int. Ed. Engl.* **2023**, *62* (36), e202302779. doi: 10.1002/anie.202302779

(40)   Fasano, A.; Fourmond, V.; Léger, C. Kinetic Modeling of 2e-/1H+ and 2e-/2H+ Bidirectional Catalytic Cycles. *Bioelectrochemistry* **2024**, *155*, 108511. doi: 10.1016/j.bioelechem.2023.108511

(41)   Fourmond, V.; Léger, C. Modelling the Voltammetry of Adsorbed Enzymes and Molecular Catalysts. *Current Opinion in Electrochemistry* **2017**, *1* (1), 110–120. doi: 10.1016/j.coelec.2016.11.002

(42)   Léger, C.; Jones, A. K.; Albracht, S. P. J.; Armstrong, F. A. Effect of a Dispersion of Interfacial Electron Transfer Rates on Steady State Catalytic Electron Transport in [NiFe]-Hydrogenase and Other Enzymes. *J. Phys. Chem. B* **2002**, *106* (50), 13058–13063. doi: 10.1021/jp0265687

(43)   Hirst, J.; Duff, J. L. C.; Jameson, G. N. L.; Kemper, M. A.; Burgess, B. K.; Armstrong, F. A. Kinetics and Mechanism of Redox-Coupled, Long-Range Proton Transfer in an Iron−Sulfur Protein. Investigation by Fast-Scan Protein-Film Voltammetry. *J. Am. Chem. Soc.* **1998**, *120* (28), 7085–7094. doi: 10.1021/ja980380c

(44)   Butt, J. N.; Jeuken, L. J. C.; Zhang, H.; Burton, J. A. J.; Sutton-Cook, A. L. Protein Film Electrochemistry. *Nature Reviews Methods Primers* **2023**, *3* (1), 1–19. doi: 10.1038/s43586-023-00262-7

(45)   Fourmond, V.; Baffert, C.; Sybirna, K.; Dementin, S.; Abou-Hamdan, A.; Meynial-Salles, I.; Soucaille, P.; Bottin, H.; Léger, C. The Mechanism of Inhibition by H2 of H2-Evolution by Hydrogenases. *Chem. Commun.* **2013**, *49* (61), 6840–6842. doi: 10.1039/c3cc43297a

(46)   Domnik, L.; Merrouch, M.; Goetzl, S.; Jeoung, J.-H.; Léger, C.; Dementin, S.; Fourmond, V.; Dobbek, H. CODH-IV: A High-Efficiency CO-Scavenging CO Dehydrogenase with Resistance to O2. *Angew. Chem. Int. Ed Engl.* **2017**, *56* (48), 15466–15469. doi: 10.1002/anie.201709261

(47)   Léger, C.; Heffron, K.; Pershad, H. R.; Maklashina, E.; Luna-Chavez, C.; Cecchini, G.; Ackrell, B. A.; Armstrong, F. A. Enzyme Electrokinetics: Energetics of Succinate Oxidation by Fumarate Reductase and Succinate Dehydrogenase. *Biochemistry* **2001**, *40* (37), 11234–11245. doi: 10.1021/bi010889b

(48)   Meneghello, M.; Uzel, A.; Broc, M.; Manuel, R. R.; Magalon, A.; Léger, C.; Pereira, I. A. C.; Walburger, A.; Fourmond, V. Electrochemical Kinetics Support a Second Coordination Sphere Mechanism in Metal-Based Formate Dehydrogenase. *Angew. Chem. Int. Ed Engl.* **2023**, *62* (6), e202212224. doi: 10.1002/anie.202212224

(49)   Hajj, V.; Baffert, C.; Sybirna, K.; Meynial-Salles, I.; Soucaille, P.; Bottin, H.; Fourmond, V.; Léger, C. FeFe Hydrogenase Reductive Inactivation and Implication for Catalysis. *Energy Environ. Sci.* **2014**, *7* (2), 715–719. doi: 10.1039/C3EE42075B

(50)   Megarity, C. F.; Esselborn, J.; Hexter, S. V.; Wittkamp, F.; Apfel, U.-P.; Happe, T.; Armstrong, F. A. Electrochemical Investigations of the Mechanism of Assembly of the Active-Site H-Cluster of [FeFe]-Hydrogenases. *J. Am. Chem. Soc.* **2016**, *138* (46), 15227–15233. doi: 10.1021/jacs.6b09366

(51)   Cunningham, D. W.; Barlow, J. M.; Velasquez, R. S.; Yang, J. Reversible and Selective CO2 to HCO2- Electrocatalysis near the Thermodynamic Potential. *Angew. Chem. Int. Ed Engl.* **2019**. doi: 10.1002/anie.201913198

(52)   Cunningham, D. W.; Yang, J. Y. Kinetic and Mechanistic Analysis of a Synthetic Reversible CO2/HCO2- Electrocatalyst. *Chem. Commun.* **2020**. doi: 10.1039/d0cc05556e

(53)   Dutta, A.; DuBois, D. L.; Roberts, J. A. S.; Shaw, W. J. Amino Acid Modified Ni Catalyst Exhibits Reversible H2 Oxidation/production over a Broad pH Range at Elevated Temperatures. *Proc. Natl. Acad. Sci. U. S. A.* **2014**, *111* (46), 16286–16291. doi: 10.1073/pnas.1416381111

(54)   Hessin, C.; Schleinitz, J.; Le Breton, N.; Choua, S.; Grimaud, L.; Fourmond, V.; Desage-El Murr, M.; Léger, C. Assessing the Extent of Potential Inversion by Cyclic Voltammetry: Theory, Pitfalls, and Application to a Nickel Complex with Redox-Active Iminosemiquinone Ligands. *Inorg. Chem.* **2023**, *62* (8), 3321–3332. doi: 10.1021/acs.inorgchem.2c04365

(55)   Kuchenreuther, J. M.; Grady-Smith, C. S.; Bingham, A. S.; George, S. J.; Cramer, S. P.; Swartz, J. R. High-Yield Expression of Heterologous [FeFe] Hydrogenases in Escherichia Coli. *PLoS One* **2010**, *5* (11), e15491. doi: 10.1371/journal.pone.0015491

(56)   Esselborn, J.; Lambertz, C.; Adamska-Venkates, A.; Simmons, T.; Berggren, G.; Noth, J.; Siebel, J.; Hemschemeier, A.; Artero, V.; Reijerse, E.; Fontecave, M.; Lubitz, W.; Happe, T. Spontaneous Activation of [FeFe]-Hydrogenases by an Inorganic [2Fe] Active Site Mimic. *Nat. Chem. Biol.* **2013**, *9* (10), 607–609. doi: 10.1038/nchembio.1311

(57)   Léger, C.; Dementin, S.; Bertrand, P.; Rousset, M.; Guigliarelli, B. Inhibition and Aerobic Inactivation Kinetics of Desulfovibrio Fructosovorans NiFe Hydrogenase Studied by Protein Film Voltammetry. *J. Am. Chem. Soc.* **2004**, *126* (38), 12162–12172. doi: 10.1021/ja046548d

(58)   Morrison, T. J.; Billett, F. 730. The Salting-out of Non-Electrolytes. Part II. The Effect of Variation in Non-Electrolyte. *J. Chem. Soc.* **1952**, No. 0, 3819–3822. doi: 10.1039/JR9520003819

(59)   Morrison, T. J. 729. The Salting-out of Non-Electrolytes. Part I. The Effect of Ionic Size, Ionic Charge, and Temperature. *J. Chem. Soc.* **1952**, No. 0, 3814–3818. doi: 10.1039/JR9520003814

(60)   White, S. F.; Turner, A. P. F.; Schmid, R. D.; Bilitewski, U. Investigations of Platinized and Rhodinized Carbon Electrodes for Use in Glucose Sensors. **1994**.

(61)   Léger, C.; Jones, A. K.; Roseboom, W.; Albracht, S. P. J.; Armstrong, F. A. Enzyme Electrokinetics: Hydrogen Evolution and Oxidation by Allochromatium Vinosum [NiFe]-Hydrogenase. *Biochemistry* **2002**, *41* (52), 15736–15746. doi: 10.1021/bi026586e

(62)   Fourmond, V. QSoas: A Versatile Software for Data Analysis. *Anal. Chem.* **2016**, *88* (10), 5050–5052. doi: 10.1021/acs.analchem.6b00224

Kinetic modeling of the reversible or irreversible electrochemical responses of FeFe-hydrogenases

Supplementary information

Andrea Fasano[a], Carole Baffert[a], Conrad Schumann[b], Gustav Berggren[b], James A. Birrell[c], Vincent Fourmond[a], Christophe Léger[a*]

a. Laboratoire de Bioénergétique et Ingénierie des Protéines. CNRS, Aix Marseille Université, UMR 7281. Marseille. France.

b. Molecular Biomimetics, Department of Chemistry, Ångström Laboratory, Uppsala University, 75120 Uppsala, Sweden

c. School of Life Sciences, University of Essex, Wivenhoe Park, Colchester, CO4 3SQ, UK

Section S1. FTIR titrations

Section S1.1 Analysis of the FTIR data

The fraction of each species shown in figure 2B of the main text was computed assuming that the total sample of enzyme exists in any (or in a mixture) of the following four spectroscopic states: H_{ox}, H_{red}, $H_{red}H^+$ and $H_{sred}H^+$. The sum of the absorbances at the specific wavenumber of each state (1939 cm^{-1}, 1933 cm^{-1}, 1891 cm^{-1} and 1881 cm^{-1},

respectively) is directly correlated with the total amount of enzyme in the sample, from which the fraction of each state was calculated according to the absorbance of the specific bands. No correction for the extinction coefficient was performed since the sum of the absorbances at the wavenumber of each four species is constant at every pH (figure S1.1), suggesting that these four species have very similar extinction coefficients.
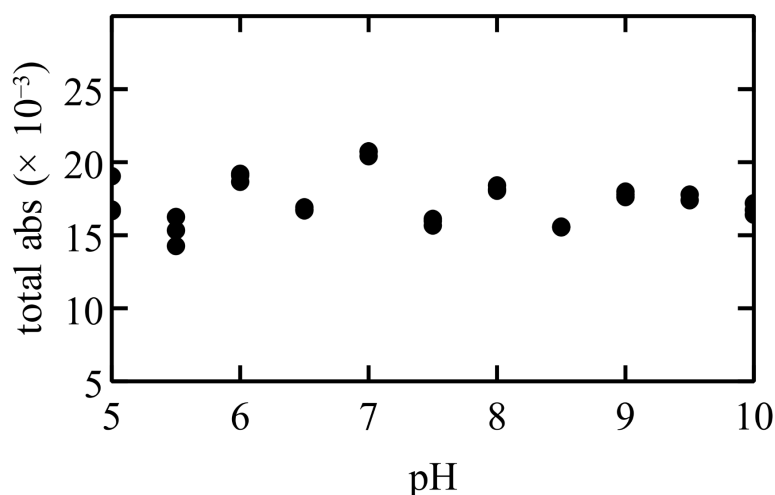

Figure S1.1: sum of the absorbances of the four spectroscopic species H_{ox} (1939 cm^{-1}), H_{red} (1933 cm^{-1}), $H_{red}H^+$ (1891 cm^{-1}) and $H_{sred}H^+$ (1881 cm^{-1}) at every pH.

Section S1.2 Modeling

We have used a simplified version of the six states model in figure 3 of ref [1]. Two of those states are predicted to exist only at very extreme conditions, and have not actually been observed ($H_{ox}H^+$ probably only forms at very low pHs and high potentials and H_{sred} at very high pH and low potentials), which we do not reach in our titration in figure 2 of the main text. The model considers therefore only the redox transition between H_{ox} and H_{red} (reduction potential $E^{0'}_1$); the protonation equilibrium between H_{red} and $H_{red}H^+$, defined by the acidity dissociation constant K; the second redox transition $H_{red}H^+/H_{sred}H^+$ (reduction potential $E^{0'}_2$).

The ratio H_{ox}/H_{red} and $H_{red}H^+/H_{sred}H^+$ is defined by the Nernst equation as:

$$\frac{[H_{ox}]}{[H_{red}]} = \exp\left(\frac{F}{RT}(E - E_0^1)\right) = e_1$$

$$\frac{[H_{red}H^+]}{[H_{sred}H^+]} = \exp\left(\frac{F}{RT}(E - E_0^2)\right) = e_2$$

The definition of the acidity constant K implies that

$$[H_{red}] = \frac{[H_{red}H^+] \times K}{[H^+]}$$

We note C_0 the total concentration of enzyme:

$$[\mathrm{H_{ox}}] + [\mathrm{H_{red}}] + [\mathrm{H_{red}H^+}] + [\mathrm{H_{sred}H^+}] = C_0$$

Substituting in the last equation each of the terms with the previous definitions and solving it per each species gives the relative populations of each of the four states. A precise description of the entire procedure is in ref [2].

$$[\mathrm{H_{ox}}] = \frac{C_0}{1 + \frac{1}{e_1} + \frac{[\mathrm{H^+}]}{Ke_1} + \frac{[\mathrm{H^+}]}{Ke_1e_2}}$$

$$[\mathrm{H_{red}}] = \frac{C_0}{1 + e_1 + \frac{[\mathrm{H^+}]}{K} + \frac{[\mathrm{H^+}]}{Ke_2}}$$

$$[\mathrm{H_{red}H^+}] = \frac{C_0}{1 + \frac{1}{e_2} + \frac{K}{[\mathrm{H^+}]} + \frac{Ke_1}{[\mathrm{H^+}]}}$$

$$[\mathrm{H_{sred}H^+}] = \frac{C_0}{1 + e_2 + \frac{Ke_2}{[\mathrm{H^+}]} + \frac{Ke_1e_2}{[\mathrm{H^+}]}}$$

Section S2. Electrochemistry

Section S2.1 (De)protonation in the 2$^{\mathrm{nd}}$ chemical step (k_2, k_{-2})

We assume that the proton is transferred from a proton relay, in the second chemical step

$$k_{+2} = \frac{k_{+2}^{\mathrm{max}}}{1 + \frac{K_{\mathrm{relay}}}{[H^+]}}$$

$$k_{-2} = \frac{k_{-2}^{\mathrm{max}}}{1 + \frac{[H^+]}{K_{\mathrm{relay}}}}$$

The equations giving E_{cat} and I_{lim} as a function of pH are like eqs 11-14 in the main text. This implies that fitting the experimental data (figure 3 panel B, C, H and I) assuming a protonation in the first or second chemical step returns equally good fits. The difference is in the definition of the apparent potentials and pKs, and therefore on the constraints on the values of the parameters that result.

$$E_1^{0\mathrm{app}} = E_1^0 + \frac{RT}{F} \ln\left[\frac{k_{-1}}{k'_{-2} + k_{-1}}\right]$$

$$E_2^{0\mathrm{app}} = E_2^0 + \frac{RT}{F} \ln\left[\frac{k_1 + k_{-1}}{k_{-1}}\right]$$

$$K_1 = K_{relay} \times \frac{k'_{-2} + k_{-1}}{k'_2 + k_{-1}}$$

$$K_2 = K_{relay} \times \frac{k_{-1}}{k'_2 + k_{-1}}$$

$$K_3 = K_{relay} \times \frac{k_1 + k_{-1}}{k'_2 + k_1 + k_{-1}}$$

$$\alpha = \frac{k'_{-2} k_{-1}}{k'_{-2} + k_{-1}}$$

$$\beta = \frac{k'_2 k_1}{k'_{-2} + k_1 + k_{-1}}$$

(Note that these parameters $E^0_1{}^{app}$, $E^0_2{}^{app}$ and the apparent acidity constants K_1, K_2, and K_3 are not the same as in eqs 17-20 and 26 in the main text.) The above definitions imply that $pK_1 < pK_2$ and $pK_3 < pK_2$, and the pH dependence of the catalytic potentials can only be fitted with $pK < pK_1 < pK_2$ ($E_{cat}{}^{ox}$) and $pK < pK_3 < pK_2$ ($E_{cat}{}^{red}$). The values of the resulting best parameters are listed in table S2.1. As mentioned in the main text, for Cr HydA1 a pK<5 (Table S2.1) is not consistent with spectroelectrochemical pH titration[1] and the H_2 pressure and pH titrations performed without electrochemical control of the potential (Figure 2 in the main text and ref [3]), which both return pK ≈ 7.2. We also consider a pK < 4 for Tam HydS inconsistent with the fact that the enzyme is active over a large range of pHs[4] and that modeling H_2 binding in the first chemical step does not fit the experimental data (section S2.2).

	E^{0app}_1 (mV)	E^{0app}_2 (mV)	pK	pK_1	pK_2	pK_3
Cr HydA1	-466	-321	<5	<5	8.3	7.9
Tam HydS	-332	-377	<4	<3.5	7.1	5.1

Table S2.1 Values of the apparent potentials and pK when assuming that the pronation occurs in the second chemical step.

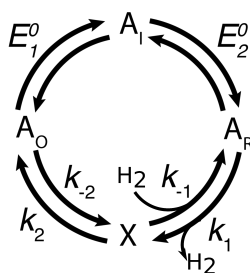## Section S2.2 H_2 binding/release in the 1st chemical step (k_1 and k_{-1})

Figure S2.1: general scheme of the EECC model, in which H_2 binding/release occurs in the first chemical step. The rate constants have a negative subscript in the direction of H_2 oxidation and a positive subscript in the direction of H_2 evolution: k_{-1} is the pseudo-1st order rate constant of H_2 binding and k_1 the 1st order rate constant of H_2 release.

In this section, we discuss the equations for E_{cat} and I_{lim} as a function of $[H_2]$, when it is assumed that H_2 binding and release occur in chemical step 1 (figure S2.1).

$$k_1 = \mathrm{cst}$$

$$k_{-1} = k'_{-1} \times [H_2]$$

The changes in E_{cat} and I_{lim} as a function of $[H_2]$ are

$$i_{\mathrm{lim}}^{\mathrm{ox}} = 2FA\Gamma \frac{k_{-2}}{1 + \frac{K_M}{[H_2]}}$$

$$i_{\mathrm{lim}}^{\mathrm{red}} = -2FA\Gamma \frac{\frac{k_1 k_2}{k_1 + k_2}}{1 + \frac{[H_2]}{K_i}}$$

$$E_{\mathrm{cat}}^{\mathrm{ox}} = E_1^{\mathrm{0app}} - \frac{RT}{F} \ln \left[\frac{1 + \frac{[H_2]}{K_M}}{1 + \frac{[H_2]}{K_b}} \right]$$

$$E_{\mathrm{cat}}^{\mathrm{red}} = E_2^{\mathrm{0app}} + \frac{RT}{F} \ln \left[\frac{1 + \frac{[H_2]}{K_i}}{1 + \frac{[H_2]}{K_b}} \right]$$

with:

$$E_1^{\mathrm{0app}} = E_1^{0\prime} - \frac{RT}{F} \times \frac{k_2 + k_{-2}}{k_2}$$

$$E_2^{\mathrm{0app}} = E_2^{0\prime} + \frac{RT}{F} \times \frac{k_2 + k_1}{k_2}$$

$$K_M = \frac{k_2 + k_{-2}}{k'_{-1}}$$

$$K_i = \frac{k_2 + k_1}{k'_{-1}}$$

$$K_b = \frac{k_2}{k'_{-1}}$$

(Note that these parameters $E_1^{0\,\mathrm{app}}$, $E_2^{0\,\mathrm{app}}$ and K_M are not the same as in eqs 17, 26 and 27 in the main text.) The above relations imply the following constraints: $K_M > K_b$ and $K_i > K_b$.

Figure S2.2 shows how this model fits the experimental data (red and orange dashed line) and compares with the best fit obtained by assuming H_2 binding in chemical step 2 (black,

same fit as that shown in figure 3 of the main text). The red lines are obtained fitting the limit case in which $K_b = K_M$ (0.3 mM in Cr HydA1 and 0.6 mM in Tam HydS), while the orange lines show the fit when K_b is forced to be smaller than K_M (K_b=0.05 mM in Cr HydA1 and K_b = 0.5 mM in Tam HydS). The limiting currents are fitted equally well by assuming H_2 binding in chemical step 1 and 2: the equation for i_{lim}^{ox} is the same (the definition of K_M as a function of the rate constant changes), which allows the fitting of both models to precisely determine the value of K_M. Assuming H_2 binding in step -1 renders the equation of i_{lim}^{red} more complex than having H_2 binding in step -2. The former model indeed predicts that the proton reduction activity is inhibited by H_2 with an inhibition constant K_i. FeFe-hydrogenases are known to be inhibited by H_2 but the inhibition constant is much greater than the H_2 concentration under saturating conditions. The parameter K_i was then fixed to 4 mM in Cr, as measured in ref 5, and 4 mM for Tam HydS as well.

The H_2 dependence of the E_{cat} is, instead, not reproduced by assuming H_2 binding in step k_{-1} (figure S2.2 panels A and B, orange and red curves). In particular, the model predicts an increase in E_{cat}^{ox} as a function of $[H_2]$ that is in contrast with the results of experiments, which confirms that H_2 binding happens in the chemical step 2 for both Cr HydA1 and Tam HydS. The same conclusion is reached assuming more complex kinetics of H_2 binding and release (SI section S2.3).
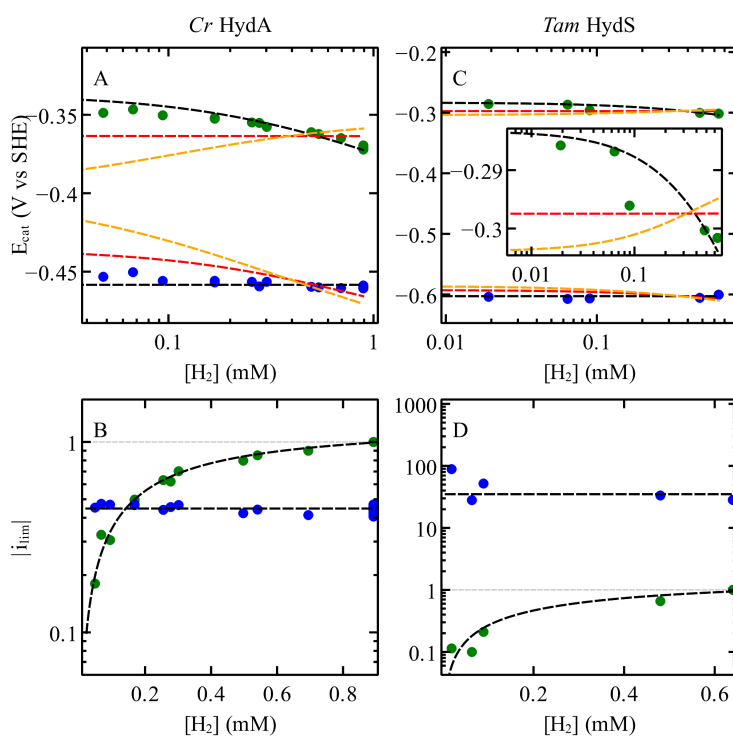

Figure S2.2 Fitting the $[H_2]$ pressure dependence of E_{cat} and I_{lim} for Cr HydA1 (panel A and B) and Tam HydS (panel C and D). The experimental data are the same as in figure 3 panels E, F, M and N (main text). E_{cat}^{ox} and I_{lim}^{ox} are shown in green, E_{cat}^{red} and I_{lim}^{red} in blue. The black dotted trace is the best fit obtained assuming unimolecular H_2 binding in step -2, as shown in figure 3 of the main text. The red and orange dashed lines are two fits of the model that assumes bimolecular H_2 binding in step -1 (the equations in section S2.2). The red line is the limit in which $K_b = K_M$ (0.3 mM for Cr HydA1 and 0.6 mM for Tam HydS), the

orange line is the fit obtained having $K_b < K_M$ (Kb=0.05 mM for Cr HydA1 and K_b = 0.5 mM for Tam HydS). K_i was fixed to 4 mM for Cr HydA1, as measured in ref [5], and to 4 mM for Tam as well.

Note that this model for H_2 binding/release in chemical step 1, combined with the model of (de)protonation in chemical step 2 (section S2.1), are an approximation of model 2 in figure 1 of the main text, in which one only considers the cycle between active species (solid arrows), forgetting about the inactivating branches. From the results in this section and in section S2.1 we conclude that assuming H_2 binding/release in the 1st chemical step and (de)protonation in the 2nd is not consistent with the experimental data for Cr HydA1 and Tam HydS.

Section S2.3 The kinetics of H_2 binding and release

In this section we describe a model for H_2 binding and release with more complex kinetics than that used in the main text. We consider a model similar to that proposed in ref [6], where the ligand diffuses through the enzyme and binds first close to the active site, to form a state that is called the geminate state, and then to the active site. Assuming that the diffusion step is fast compared to H_2 binding/release at the active site, we obtain the following expressions for the rate constants of hydrogen binding (k-) and release (k+):

$$k_+ = \frac{k_+^{\mathrm{max}}}{1 + \frac{[H_2]}{K_G}}$$

$$k_- = \frac{k_-^{\mathrm{max}}}{1 + \frac{K_G}{[H_2]}}$$

Where K_G is the dissociation constant of the H_2 in the geminate state.

Substitution of the above two equations in the definition of E_{cat} and I_{lim} (eqs 3-6 in the main text), and assuming that H_2 binding/release occurs in step 1 or 2 gives:

$$i_{\mathrm{lim}}^{\mathrm{ox}} = \frac{\alpha}{1 + \frac{K_M}{[H_2]}}$$

$$i_{\mathrm{lim}}^{\mathrm{red}} = \frac{\beta}{1 + \frac{[H_2]}{K_i}}$$

$$E_{\mathrm{cat}}^{\mathrm{ox}} = E_1^{0\mathrm{app}} + \frac{RT}{F} \ln \left[\frac{1 + \frac{[H_2]}{K_1}}{1 + \frac{[H_2]}{K_M}} \right]$$

$$E_{\mathrm{cat}}^{\mathrm{red}} = E_2^{0\mathrm{app}} + \frac{RT}{F} \ln \left[\frac{1 + \frac{[H_2]}{K_i}}{1 + \frac{[H_2]}{K_1}} \right]$$

with definitions of the parameters in Table S2.2. (Note that these parameters $E^0_1{}^{app}$, $E^0_2{}^{app}$ and K_M are not the same as in eqs 17, 26 and 27 in the main text.)

	Model 1 (H$_2$ binding/release in C1)	Model 2 (H$_2$ binding/release in C2)
$\mathrm{E}_1^{0\mathrm{app}}$	$\mathrm{E}_1^{0\prime} + \dfrac{RT}{F} \ln \left[\dfrac{k_2}{k_2 + k_{-2}} \right]$	$\mathrm{E}_1^{0\prime}$
$\mathrm{E}_2^{0\mathrm{app}}$	$\mathrm{E}_2^{0\prime} + \dfrac{RT}{F} \ln \left[\dfrac{k_2 + k_1'}{k_2} \right]$	$\mathrm{E}_2^{0\prime} + \dfrac{RT}{F} \ln \left[\dfrac{k_2 + k_1'}{k_2} \right]$
K_1	$K_G \times \dfrac{k_2}{k_2 + k_{-1}'}$	$K_G \times \dfrac{k_2' + k_{-1}}{k_{-1}}$
K_M	$K_G \times \dfrac{k_2 + k_{-2}}{k_2 + k_{-2} + k_{-1}'}$	$K_G \times \dfrac{k_2' + k_{-1}}{k_{-2}' + k_{-1}}$
K_i	$K_G \times \dfrac{k_2 + k_1'}{k_2 + k_{-1}'}$	$K_G \times \dfrac{k_2' + k_1 + k_{-1}}{k_1 + k_{-1}}$
α	$2FA\Gamma \dfrac{k_2 k_{-1}'}{k_2 + k_{-2} + k_{-1}'}$	$2FA\Gamma \dfrac{k_{-2}' k_{-1}}{k_{-2}' + k_{-1}}$
β	$-2FA\Gamma \dfrac{k_2 k_1'}{k_2 + k_1'}$	$-2FA\Gamma \dfrac{k_2' k_1}{k_2' + k_1 + k_{-1}}$
constraint	$K_1 < K_m$ $K_1 < K_i$	$K_1 > K_m$ $K_1 > K_i$

Table S2.2: Definition of the apparent potential and dissociation constant for H$_2$ binding/release in the first (model 1) or second (model 2) chemical step.

Figure S2.3 shows the best fits of the two models of table S2.2 to the experimental data shown in figure 3 panels E, F, M and N of the main text. Again the equations describing the limiting currents are the same for all the models and therefore fit equally well the data, allowing the measurement of K_M, the Michaelis constant, and K_i, the inhibition constant of proton reduction. As discussed in section S2.2 the value of K_i is high, and we therefore fixed it to 4 mM. Assuming this more complex kinetics of H$_2$ binding and release therefore does not change the conclusion drawn by simply assuming bimolecular H$_2$ binding and unimolecular H$_2$ release (main text and SI section S2.2). Indeed, only model 2, which assumes H$_2$ binding and release in chemical step 2, fits the data well (black dashed lines in figure S2.2). Model 1 was fitted in the limiting case in which $K_1 = K_M$ (red dashed lines) and when $K_1 < K_M$ (orange lines), and in both cases the H$_2$ dependence of the E$_{cat}$ is not reproduced by the model, confirming that H$_2$ binding and release occur in the second chemical step.
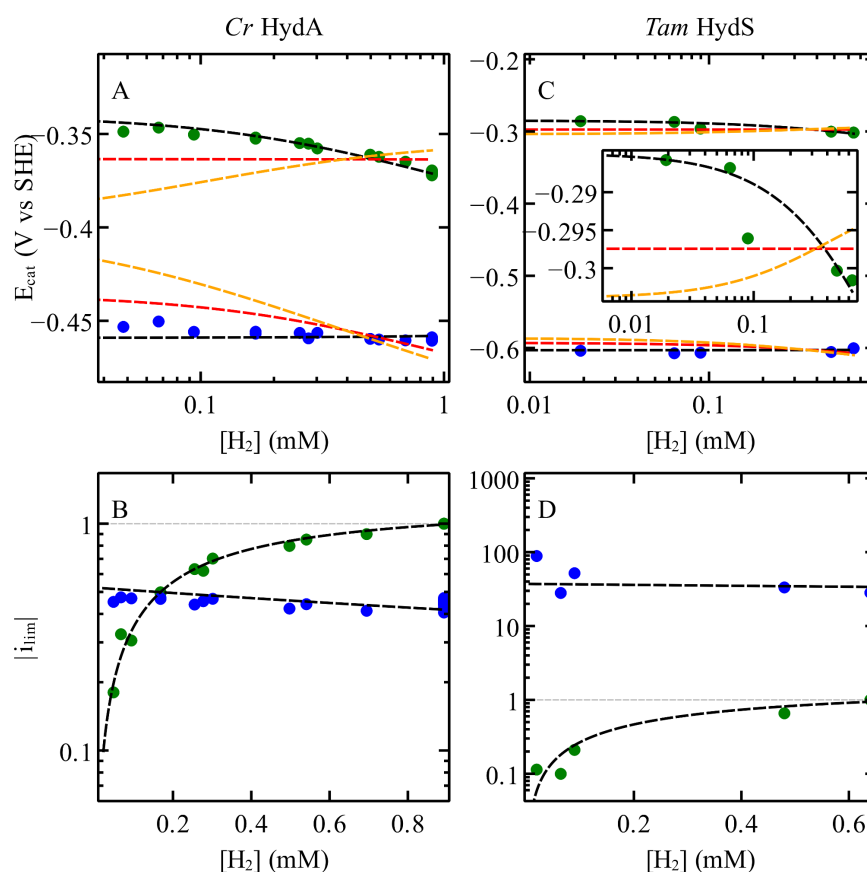
Figure S2.3 Fitting the H_2 pressure dependence of E_{cat} and I_{lim} for Cr HydA1 (panel A and B) and Tam HydS (panel C and D) considering the geminate state. E_{cat}^{ox} and I_{lim}^{ox} are shown in green, E_{cat}^{red} and I_{lim}^{red} in blue. The experimental data are the same as of figure 3 panels E, F, M and N. The black dash trace is the best fit obtained fitting model 2 (H_2 binding/release in the second chemical step). The red and orange dashed lines are obtained fitting model 1 (H_2 binding/release in the second chemical step). The red line is the limit in which $K_1 = K_M$ (0.3 mM for Cr HydA1 and 0.6 mM for Tam HydS), the orange line is the fit obtained having $K_1 < K_M$ (K_1=0.05 mM for Cr HydA1 and K_1=0.5 mM for Tam HydS). K_i was fixed to 4 mM for Cr HydA1, as measured in ref [5], and to 4 mM for Tam HydS as well. When fitting model 2 K_1 has to be larger than K_i and was therefore fixed to 5 mM in Cr HydA1 and 11 mM in Tam HydS.

Section S2.4 Relation between the acidity constant for the second protonation and K₃

The second protonation of the catalytic cycle occurs in the first chemical step and is the following reaction:

$$H_{sred}H^+ + H^+ \leftrightarrows H_{hyd}H^+$$
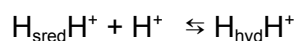
Note that $H_{sred}H^+$ is only protonated once, while $H_{hyd}H^+$ is doubly protonated.
k_1 in the catalytic cycle is therefore the rate constant for the formation of $H_{hyd}H^+$ (protonation) and k_{-1} the rate constant for formation of $H_{sred}H^+$ (deprotonation).

The acidity constant K_a is therefore:

$$K_a = \frac{[\mathrm{H_{sred}H^+}] \times [\mathrm{H^+}]}{[\mathrm{H_{hyd}H^+}]} = \frac{k_{-1}}{k_1} \times [\mathrm{H^+}]$$

Introducing the kinetics of protonation defined in equations 9 and 10 of the main text, we obtain:

$$\frac{K_a}{[\mathrm{H^+}]} = \frac{k_{-1}^{max}}{1 + \frac{[\mathrm{H^+}]}{K_{relay}}} \times \frac{1 + \frac{K_{relay}}{[\mathrm{H^+}]}}{k_1^{max}}$$

which can be simplified in

$$K_a = \frac{k_{-1}^{max}}{k_1^{max}} \times K_{relay}$$

The definition of K_3 in equation 18 of the main text corresponds to K_a if k_2 is much smaller than the (de)protonation rate constants.

## Section S2.5 Modeling of E_{cat} and i_{lim} as a function of pH at 5°C for Cr HydA1
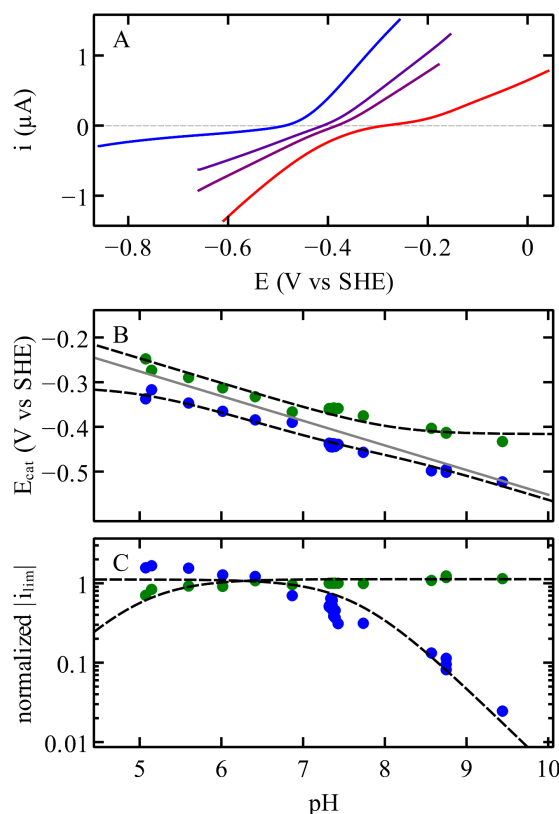
Figure S2.4: Cyclic voltammograms, catalytic potentials and limiting currents at different pHs for Cr HydA1 at 5°C The black dashed lines are the best fits of eqs 11-14 of the main text. The parameters are shown in Table S2.3. Panel A shows selected blank subtracted, averaged, cyclic voltammograms for Cr HydA1 at different pHs (at 1 atm [H₂], 5°C). Colors go from blue to red from high to low pH (pH values are 5.1, 6.9, 7.4, 8.8). Other

conditions: scan rate 20 mV/s, electrode rotation rate 3000 rpm. The catalytic potentials and the normalized limiting currents are plotted as a function of pH (panels B and C). The current values were normalized by the value of i_{lim}^{ox} at pH 7 in the plots of i_{lim} against pH. In green E_{cat}^{ox} and i_{lim}^{ox}, in blue E_{cat}^{red} and i_{lim}^{red}. In panel B a solid gray line indicates the Nernst potential of the H^+/H_2 couple.

	E^{0app}_1 (mV)	E^0_2 (mV)	pK	pK_1	pK_2	pK_3
Cr HydA1 5°C	-416	-457	8.1	< 5	< 5	7.7
Cr HydA1 30°C	-466	-523	8.3	< 5	< 5	7.9

Table S2.3: Parameters obtained by fitting eqs 11-14 (main text) to the data shown in figure S2.3, to interpret the pH-dependence of the catalytic potentials and limiting currents. The values at 30°C are repeated here to ease the comparison.
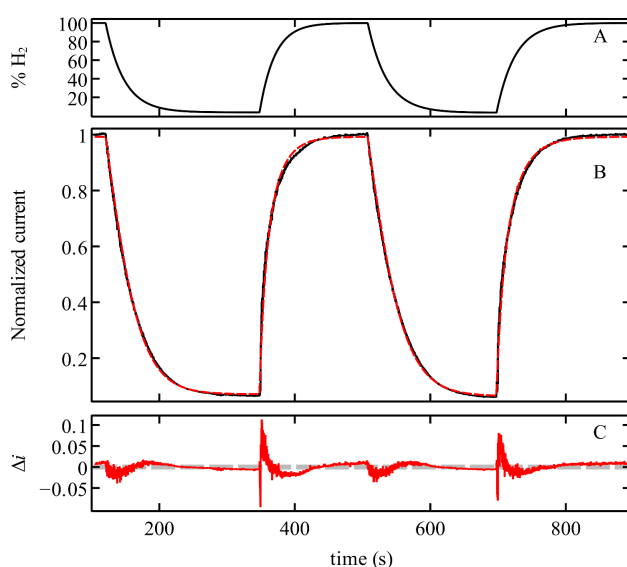
Section S2.6 Tam HydS K_M measurement

Figure S2.5: Measurement of the Michaelis constant of Tam HydS. Panel A shows the partial pressure of H_2 as a function of time in the experiment. Panel B shows the resulting catalytic current in solid black line and the fit of the Michaelis-Menten equation in dashed red line. The obtained value of K_M is 1 atm (which corresponds to 0.64 mM, considering the solubility of H_2 at 40°C). Panel C shows the difference between the data and the fit. Experimental conditions: -59 mV vs SHE; 40°C; pH 6.5; 3000 rpm.

Section S2.7 Modeling of the cyclic voltammograms of Cr HydA1 recorded at different pH values
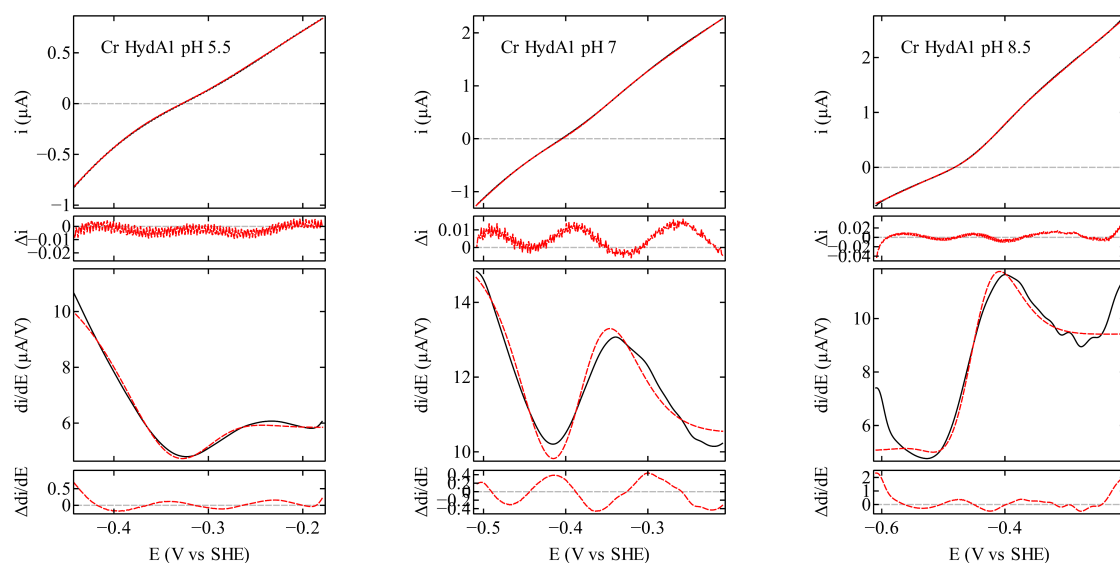

Figure S2.6: Fits of the generic EEC model to the voltammograms obtained with Cr HydA1 at pH 5.5, 7 and 8.5, from left to right. The top panel shows the experimental data in black solid lines and the fit in red dash lines. The residual (difference between data and fit) is shown in red in the panel below. The bottom panel shows the derivative of the data in black solid lines and the fit in dash red lines. Again, the residual is shown in the bottom panel. The capacitive current recorded without enzyme was subtracted from all the voltammograms. The 2 scans were then averaged. Conditions: scan rate 20 mV/s; 3000 rpm; at 30°C.

Section S2.8 Modeling of the voltammograms recorded with Cr HydA1 at different concentrations of H$_2$.
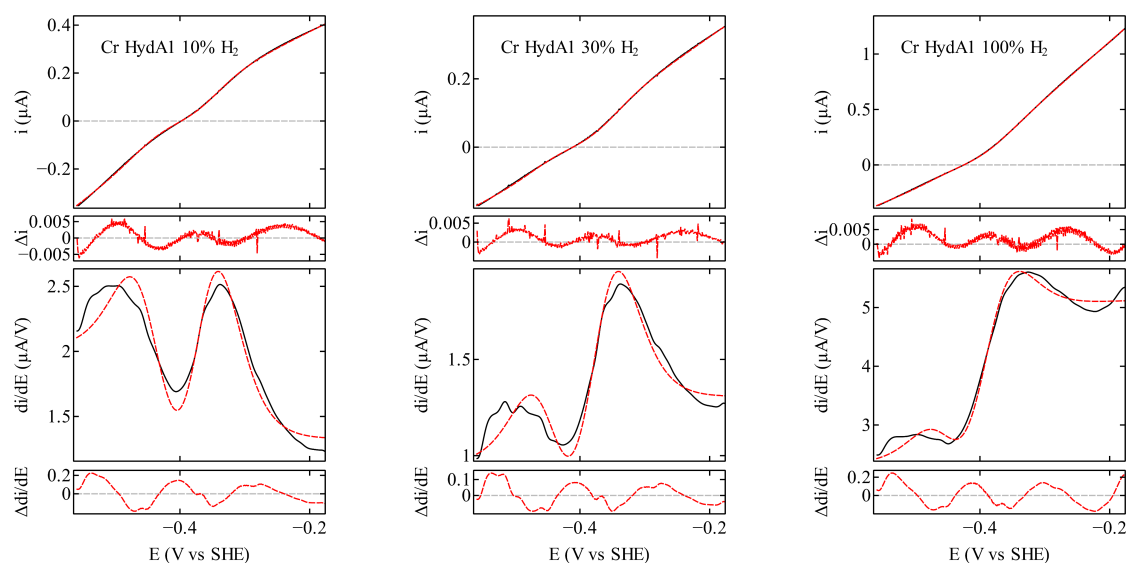

Figure S2.7: Fits of a generic EEC model to the voltammograms obtained with Cr HydA1 at pH 7.7, under 10, 30 and 100 % of H$_2$ from left to right. The top panel shows the experimental data in black solid lines and the fit in red dash lines. The residual (difference between data and fit) is shown in red in the panel below. The bottom panel shows the derivative of the data in black solid lines and the fit in dash red lines. Again the residual is shown in the panel below. The capacitive current recorded without enzyme was subtracted from all the voltammograms. The 2 scans were then averaged. Conditions: scan rate 20 mV/s; 3000 rpm; at 5°C.

Section S2.9 Modeling of the voltammograms recorded with Tam HydS at different concentrations of H_2

To analyse the voltammetry of Tam HydS at different H_2 pressures (figures S2.8, S2.9 and 2.10) one has to deal with the fact that the reductive current has much greater intensity than the oxidative current, especially at low H_2 partial pressure. To properly fit the model to the oxidative part of the voltammogram, we proceeded by analysing first the complete signal (panels A to D in figures S2.8, S2.9 and 2.10) to obtain the value of E_{cat}^{red}. The high potential part was then analyzed separately (panels E to H in figures S2.8, S2.9 and 2.10) to obtain the value of E_{cat}^{ox} as precisely as possible.
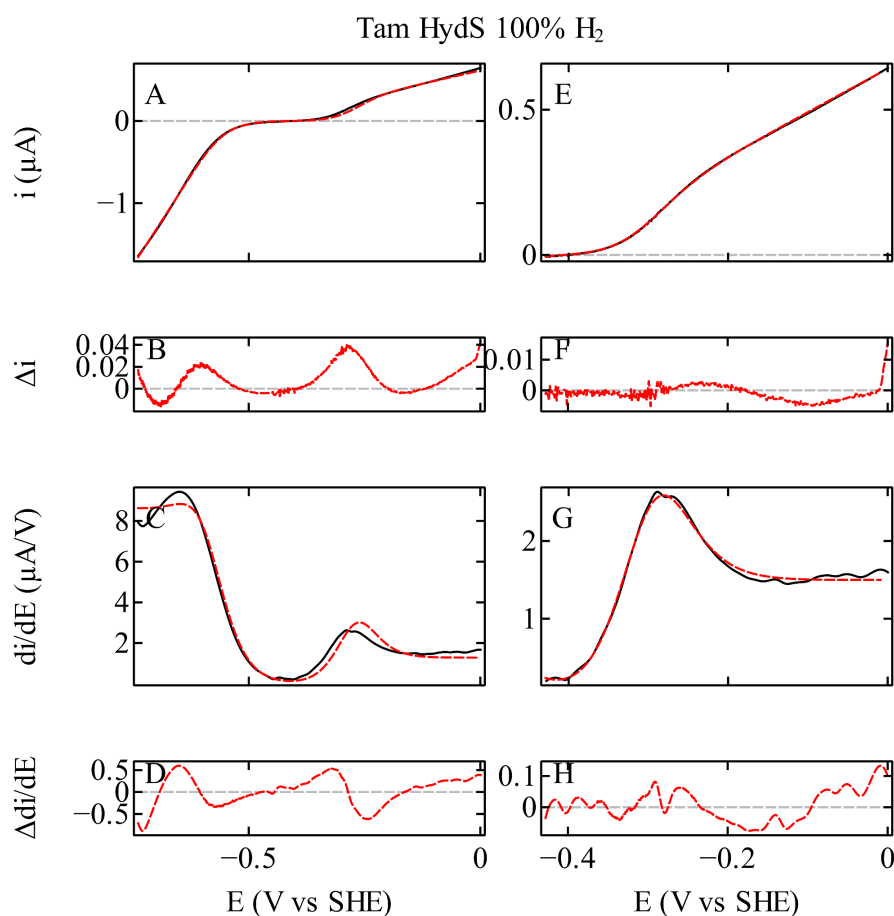

Figure S2.8: Fits of a generic EEC model to the voltammograms of Tam HydS at pH 6.5, under 100% H_2. The left column panels show the fit of the model to the entire CV, the right column panels show the analysis of the high potential part only. Panels A and E show the experimental data in black solid lines and the fit in red dash lines. The residual (difference between data and fit) is shown in red in the bottom panels (B and F). Panels C and G show the derivative of the data in black solid lines and the fit in dash red lines. Again, the residual is shown in the bottom panels (D and H). The capacitive current recorded without enzyme was subtracted from all the voltammograms. The 2 scans were then averaged. Conditions: scan rate 20 mV/s; 3000 rpm; at 40°C.
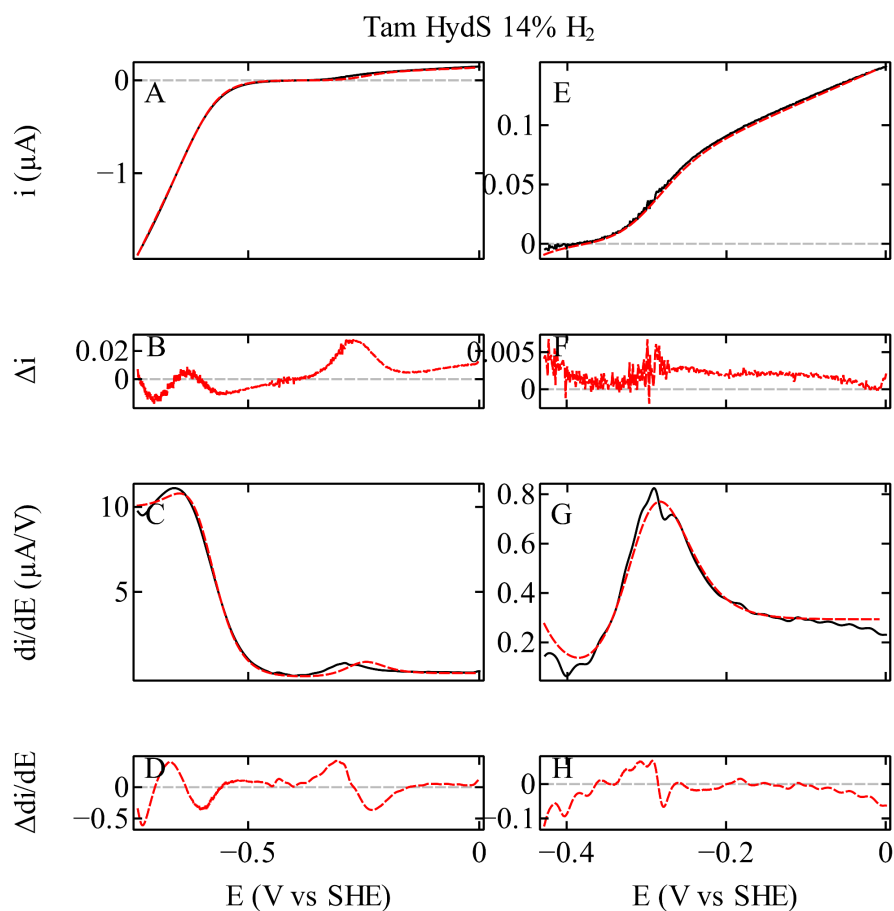
Figure S2.9: Fits of a generic EEC model to the voltammograms recorded with Tam HydS under pH 6.5, under 14% H_2 The left column panels show the fit of the model to the entire CV, the right column panels show the analysis of the high potential part only. Conditions: scan rate 20 mV/s; 3000 rpm; at 40°C.
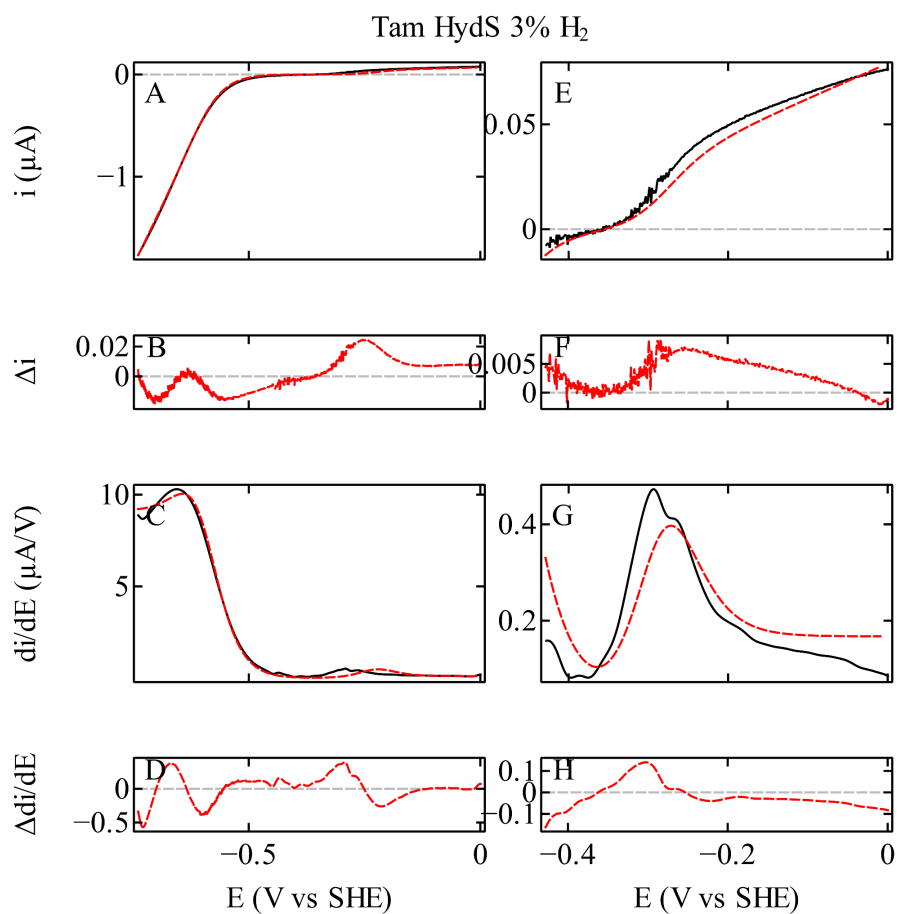
Figure S2.10: Fits of a generic EEC model to the voltammograms recorded with Tam HydS at pH 6.5, under 3% H_2 Conditions: scan rate 20 mV/s; 3000 rpm; at 40°C.

S2.10 Modeling the (de)protonation events for an ECEC kinetic scheme

The equation defining the catalytic potential and limited current in the case of an ECEC kinetic scheme were derived in ref [7] and copied below:

$$E_{\text{cat}}^{\text{ox}} = \frac{RT}{F} \ln \left[\frac{(k_1 + k_{-1}) \exp \frac{FE_0^1}{RT} + (k_2 + k_{-2}) \exp \frac{FE_0^2}{RT}}{k_{-1} + k_{-2}} \right]$$

$$E_{\text{cat}}^{\text{red}} = -\frac{RT}{F} \ln \left[\frac{(k_1 + k_{-1}) \exp \frac{-FE_0^2}{RT} + (k_2 + k_{-2}) \exp \frac{-FE_0^1}{RT}}{k_1 + k_2} \right]$$

$$i_{\text{lim}}^{\text{ox}} = 2FA\Gamma \frac{k_{-1}k_{-2}}{k_{-1} + k_{-2}}$$

$$i_{\text{lim}}^{\text{red}} = -2FA\Gamma \frac{k_1 k_2}{k_1 + k_2}$$

Protonation kinetics such as that described by equations 9 and 10 of the main text was included in the 2 chemical steps, giving the following dependences of the catalytic potentials and limiting currents on pH:

$$E_{\text{cat}}^{\text{ox}} = E_0^{1\text{app}} + \frac{RT}{F} \ln \left(1 + \frac{[\text{H}^+]}{K_1} \right)$$

$$E_{\text{cat}}^{\text{red}} = E_0^{2\text{app}} + \frac{RT}{F} \ln \left(\frac{1}{1 + \frac{K_1}{[\text{H}^+]}} \right)$$

$$i_{\text{lim}}^{\text{ox}} = 2FA\Gamma \frac{\alpha}{1 + \frac{[\text{H}^+]}{K_{relay}}}$$

$$i_{\text{lim}}^{\text{ox}} = -2FA\Gamma \frac{\beta}{1 + \frac{K_{relay}}{[\text{H}^+]}}$$

It is clear that this model cannot fit the experimental data shown in figure 3 (panels B, C, H and I): the limiting currents should both decrease 1 decade per pH unit above ($i_{\text{lim}}^{\text{red}}$) or below ($i_{\text{lim}}^{\text{ox}}$) the value of pK_{relay}, which is not something we see in the experimental data; $E_{\text{cat}}^{\text{ox}}$ should increase with a slope of -60 mV/pH at pH below pK_1 while $E_{\text{cat}}^{\text{red}}$ should decrease 60 mV/pH at pH above pK_1, again not observed in the experimental data, no matter the value of pK_1.

Below are the definition of the parameters of the previous equations:

$$E_0^{1\text{app}} = \frac{E_0^1 + \frac{RT}{F} \ln(k_{-1}^{\max}) + E_0^2 + \frac{RT}{F} \ln(k_{-2}^{\max})}{k_{-1}^{\max} + k_{-2}^{\max}}$$

$$E_0^{2\text{app}} = \frac{\left[E_0^1 + \frac{RT}{F}\ln(k_1^{\max} + k_2^{\max})\right] \times \left[E_0^2 + \frac{RT}{F}\ln(k_1^{\max} + k_2^{\max})\right]}{E_0^1 + \frac{RT}{F}\ln(k_1^{\max}) + E_0^2 + \frac{RT}{F}\ln(k_2^{\max})}$$

$$K_1 = K_{\text{relay}} \times \frac{E_0^1 + \frac{RT}{F}\ln(k_{-1}^{\max}) + E_0^2 + \frac{RT}{F}\ln(k_{-2}^{\max})}{E_0^1 + \frac{RT}{F}\ln(k_1^{\max}) + E_0^2 + \frac{RT}{F}\ln(k_2^{\max})}$$

$$\alpha = \frac{k_{-2}^{\max} k_{-1}^{\max}}{k_{-2}^{\max} + k_{-1}^{\max}}$$

$$\beta = \frac{k_2^{\max} k_1^{\max}}{k_2^{\max} + k_1^{\max}}$$

Section S3. Preparation of [2Fe]ADT- activated TamHydS

The preparation of the holo-form of TamHydS was performed as previously reported with minor changes to the procedure.[4] For the expression of the apo-form, sequence-confirmed plasmids were transformed in chemically competent E. coli BL21(DE3) cells. The cells were cultivated in sterile M9 medium (22 mM KH_2PO_4, 22 mM Na_2HPO_4, 18 mM NH_4Cl, 0.2 mM $MgSO_4$, 85 mM NaCl, 0.1 mM $CaCl_2$, 4 g L^{-1} D-glucose) at 37 °C. After reaching O.D.600 ≈ 0.5, the cultivation temperature was lowered to 20°C, and the protein expression was induced with 1 mM IPTG with concomitant supplementation of the culture with 100 µM $FeSO_4$ in 1% HCl solution. The cell pellet was harvest ≈ 16 h after induction and stored at −20 °C until lysis. The cell lysis, the protein purification, the reconstitution of the [4Fe-4S] clusters, as well as the activation of the enzyme were carried out in an MBRAUN glovebox under argon atmosphere (app. 1 ppm O_2). The cell were lysed by resuspending the pellet in lysis buffer (10 mM $MgCl_2$, 10 mg mL^{-1} lysozyme, 0.05 mg mL^{-1} RNAse and 0.05 mg mL^{-1} DNAse in 100 mM Tris-HCl, 150 mM NaCl pH 8.0) and a subsequent sonication. The protein was purified using StrepTrap affinity chromatography (StrepTrap HP (GE Healthcare)) following the manufacturer's instructions, with an additional washing step using a sub-denaturing concentration of 1 M urea in 100 mM Tris-HCl, 150 mM NaCl pH 8.0.[8,9] A subsequent size-exclusion chromatography (Superdex 200 HP (GE Healthcare)) step was performed for the removal of low molecular weight impurities. After the two purification steps, the protein yield was 0.6 mg L^{-1} of cell culture with an iron/protein content of 7 Fe/protein. By incubating the enzyme (50 µM) in a reaction with 500 µM dithiothreitol, 500 nM cysteine desulferase (E. coli IscS), 700 µM L-cysteine and 700 µM $(NH_4)_2Fe(SO_4)_2(H_2O)_6$ in 100 mM Tris-HCl, 150 mM NaCl pH 8.0 all [4Fe-4S] clusters were fully reconstituted (16.8 Fe/protein). Subsequently, the apo-form of TamHydS (50 µM) was activated by incubating it for 2 h with 1 mM sodium dithionite and 600 µM [2Fe]ADT in 100 mM phosphate buffer pH 6.8, and desalted with 10 mM Tris-HCl pH 8.0. After concentrating the generated holo-form of TamHydS, aliquots were prepared in air-tight vials, flash frozen in liquid N_2 and stored at −80 °C. The successful activation with [2Fe]ADT and the correct cofactor integration were verified by ATR-FTIR, and EPR analyses.

References

(1) Sommer, C.; Adamska-Venkatesh, A.; Pawlak, K.; Birrell, J. A.; Rüdiger, O.; Reijerse, E. J.; Lubitz, W. Proton Coupled Electronic Rearrangement within the H-Cluster as an Essential Step in the Catalytic Cycle of [FeFe] Hydrogenases. *J. Am. Chem. Soc.* **2017**, *139* (4), 1440–1443. doi: 10.1021/jacs.6b12636

(2) Birrell, J. A.; Rodríguez-Maciá, P.; Hery-Barranco, A. A Beginner's Guide to Thermodynamic Modelling of [FeFe] Hydrogenase. *Catalysts* **2021**, *11* (2), 238. doi: 10.3390/catal11020238

(3) Laun, K.; Baranova, I.; Duan, J.; Kertess, L.; Wittkamp, F.; Apfel, U.-P.; Happe, T.; Senger, M.; Stripp, S. T. Site-Selective Protonation of the One-Electron Reduced Cofactor in [FeFe]-Hydrogenase. *Dalton Trans.* **2021**, *50* (10), 3641–3650. doi: 10.1039/d1dt00110h

(4) Land, H.; Sekretareva, A.; Huang, P.; Redman, H. J.; Németh, B.; Polidori, N.; Mészáros, L. S.; Senger, M.; Stripp, S. T.; Berggren, G. Characterization of a Putative Sensory [FeFe]-Hydrogenase Provides New Insight into the Role of the Active Site Architecture. *Chem. Sci.* **2020**, *11* (47), 12789–12801. doi: 10.1039/d0sc03319g

(5) Fourmond, V.; Baffert, C.; Sybirna, K.; Dementin, S.; Abou-Hamdan, A.; Meynial-Salles, I.; Soucaille, P.; Bottin, H.; Léger, C. The Mechanism of Inhibition by H2 of H2-Evolution by Hydrogenases. *Chem. Commun.* **2013**, *49* (61), 6840–6842. doi: 10.1039/c3cc43297a

(6) Liebgott, P.-P.; Leroux, F.; Burlat, B.; Dementin, S.; Baffert, C.; Lautier, T.; Fourmond, V.; Ceccaldi, P.; Cavazza, C.; Meynial-Salles, I.; Soucaille, P.; Fontecilla-Camps, J. C.; Guigliarelli, B.; Bertrand, P.; Rousset, M.; Léger, C. Relating Diffusion along the Substrate Tunnel and Oxygen Sensitivity in Hydrogenase. *Nat. Chem. Biol.* **2010**, *6* (1), 63–70. doi: 10.1038/nchembio.276

(7) Fourmond, V.; Wiedner, E. S.; Shaw, W. J.; Léger, C. Understanding and Design of Bidirectional and Reversible Catalysts of Multielectron, Multistep Reactions. *J. Am. Chem. Soc.* **2019**, *141* (28), 11269–11285. doi: 10.1021/jacs.9b04854

(8) Belval, L.; Marquette, A.; Mestre, P.; Piron, M.-C.; Demangeat, G.; Merdinoglu, D.; Chich, J.-F. A Fast and Simple Method to Eliminate Cpn60 from Functional Recombinant Proteins Produced by E. Coli Arctic Express. *Protein Expr. Purif.* **2015**, *109*, 29–34. doi: 10.1016/j.pep.2015.01.009

(9) Cabotaje, P. R.; Walter, K.; Zamader, A.; Huang, P.; Ho, F.; Land, H.; Senger, M.; Berggren, G. Probing Substrate Transport Effects on Enzymatic Hydrogen Catalysis: An Alternative Proton Transfer Pathway in Putatively Sensory [FeFe] Hydrogenase. *ACS Catal.* **2023**, *13* (15), 10435–10446. doi: 10.1021/acscatal.3c02314